RSC Advances

PAPER

View Article Online
View Journal | View Issue

Cite this: RSC Adv., 2026, 16, 26348

Valorization of *Opuntia dillenii* biomass into a reusable bio-based composite for sustainable and efficient methyl orange adsorption

Thi-Kim-Chi Huynh, *[ab] Thi-Hong-An Nguyen,†[a] Cong-Hau Huynh,†[c] Xuan-Ngoc Nguyen,[ad] Thi-Cam-Thu Nguyen, [a] Hoang-Phuc Nguyen,[a] Anh-Khoa Ton,[ae] Thanh-Danh Nguyen,[a] Thi Be Ta Truong,[c] Nguyen Thi Thanh Tu, [f] Chien Phuong Tran[g] and Thi-Kim-Dung Hoang [a]

The discharge of dye-laden effluents from textile industries poses serious environmental and health risks, necessitating the development of efficient and sustainable adsorbents. In this study, a novel bio-based composite adsorbent (SPCA) was rationally designed and fabricated *via* the valorization of *Opuntia dillenii*-derived pectin combined with sodium alginate, chitosan, activated carbon, and eco-friendly additives. The composite was synthesized under mild conditions through dual crosslinking, involving Zn^{2+}-mediated ionic coordination and glutaraldehyde-induced covalent bonding, while sodium bicarbonate served as a green pore-forming agent to generate a hierarchical porous structure. Structural characterization (FT-IR, PXRD, SEM) confirmed the formation of an amorphous, interconnected polymeric network enriched with abundant oxygen- and nitrogen-containing functional groups. BET analysis revealed a well-developed mesoporous architecture with high surface area, and thermal analyses (TGA-DSC) demonstrated enhanced structural stability resulting from synergistic intermolecular interactions. Under optimal conditions (pH 4 and 4 h contact time), SPCA exhibited a maximum adsorption capacity of 18.55 mg g^{-1} at an initial MO concentration of 200 mg L^{-1}, while achieving 96.0% removal efficiency with a capacity of 14.38 mg g^{-1} at 150 mg L^{-1}. Kinetic studies indicated that adsorption follows a pseudo-second-order model ($R^2 = 0.9985$), suggesting chemisorption-dominated interactions, and equilibrium data were best described by the Freundlich isotherm ($R^2 = 0.9945$), confirming heterogeneous multilayer adsorption. Notably, SPCA retained 83.62% of its initial adsorption efficiency after six regeneration cycles using ethanol as a benign desorbing solvent. Overall, this work demonstrates an effective strategy for transforming underutilized cactus biomass into a reusable, environmentally benign adsorbent for dye-contaminated wastewater treatment.

Received 20th March 2026
Accepted 11th May 2026

DOI: 10.1039/d6ra02331b

rsc.li/rsc-advances

1. Introduction

Each year, an estimated 280 000 tons of synthetic dyes are discharged into natural water bodies, posing a serious and persistent threat to aquatic ecosystems and human health.[1] Since the introduction of the first synthetic dye in 1856, the rapid expansion of dye manufacturing, particularly driven by the textile, paper, leather, and plastic industries, has led to the large-scale release of highly colored, chemically stable effluents into the environment.[2] These dye-containing wastewaters are among the most challenging industrial pollutants to treat due to their complex aromatic structures, high visibility even at low concentrations, and resistance to biodegradation. Once released, dyes significantly impair water quality by reducing light penetration, suppressing photosynthetic activity, and disturbing the ecological balance of aquatic systems.[3]

Beyond their ecological impact, synthetic dyes have been widely reported to exert detrimental effects on human health.[4] Prolonged exposure to dye-contaminated water has been associated with kidney, liver, and brain dysfunction, central nervous system disorders, contact dermatitis, allergic reactions, and potential carcinogenicity.[5] Among various dye classes, azo dyes constitute the largest group, accounting for more than 70% of

---

[a] Institute of Advanced Technology, Vietnam Academy of Science and Technology, No. 1B, TL29 Street, An Phu Dong Ward, Ho Chi Minh City, Vietnam. E-mail: maihuynh1224@gmail.com

[b] Graduate University of Science and Technology - Vietnam Academy of Science and Technology, No.18, Hoang Quoc Viet Street, Nghia Do Ward, Hanoi, Vietnam

[c] Group of Applied Research in Advanced Materials for Sustainable Development, Faculty of Applied Sciences, Ton Duc Thang University, Ho Chi Minh City, Vietnam

[d] Ho Chi Minh University of Technology-Vietnam National University, Vietnam

[e] Faculty of Health Sciences, Mekong University, Vinh Long Province, Vietnam

[f] Faculty of Applied Technology, Van Lang School of Technology, Van Lang University, Ho Chi Minh City, Vietnam

[g] Institute for Tropical Technology, Vietnam

† These authors contributed equally.

global dye production.[6] Of particular concern is the fact that approximately 10–15% of azo dyes are lost during synthesis, processing, and application, leading to their uncontrolled release into wastewater streams. Due to the presence of azo (–N═N–) bonds and conjugated aromatic systems, these dyes exhibit high chemical stability and persistence, rendering conventional biological treatment processes largely ineffective.[7] Notably, methyl orange (MO), a representative anionic azo dye widely used in textile dyeing, printing, and analytical applications, is frequently detected in industrial effluents and aquatic environments.[8] Owing to its sulfonate group and extended aromatic structure, MO exhibits high water solubility and strong resistance to biodegradation, while its reductive cleavage may generate toxic aromatic amines.[9] Consequently, the development of efficient, cost-effective, and environmentally benign strategies for azo dye removal remains an urgent scientific and technological challenge.

In recent decades, adsorption has emerged as one of the most promising approaches for dye removal owing to its operational simplicity, high removal efficiency, adaptability to a wide range of pollutants, and minimal generation of secondary waste.[10,11] However, the widespread application of adsorption technology is still limited by the high cost, limited regenerability, and environmental concerns associated with conventional adsorbents such as commercial activated carbon. This has prompted increasing research interest in the development of sustainable, bio-based adsorbent materials derived from renewable resources. Natural polysaccharides, including pectin, chitosan, and alginate, have attracted considerable attention as environmentally friendly alternatives for wastewater treatment. These biopolymers are abundant, biodegradable, non-toxic, and rich in functional groups such as hydroxyl (–OH), carboxyl (–COOH), and amino (–NH_2) moieties, which can interact strongly with dye molecules through electrostatic attraction, hydrogen bonding, and other physicochemical mechanisms.[12,13] Among them, pectin has demonstrated notable potential in the adsorption of heavy metals and organic pollutants, as well as in the fabrication of biodegradable films and gels.[14–16] Nevertheless, the direct use of single-component biopolymers often suffers from drawbacks such as poor mechanical strength, limited surface area, and insufficient stability under varying environmental conditions.

To overcome these limitations, composite materials based on natural polysaccharides have been widely proposed. By integrating multiple biopolymers with complementary properties and incorporating porous fillers, composite adsorbents can achieve enhanced surface area, improved mechanical robustness, and increased density of active adsorption sites.[17,18] Importantly, such composites also offer the advantage of regenerability, allowing adsorbents to be reused over multiple adsorption–desorption cycles. This regenerability not only reduces operational costs but also significantly improves the economic and environmental sustainability of adsorption-based wastewater treatment systems, aligning with the principles of green chemistry and circular economy.

Despite these advances, the selection of sustainable and underutilized biomass sources for pectin extraction and composite fabrication remains an important research gap. Cactus plants, particularly *Opuntia dillenii*, represent a promising yet largely unexplored resource in this context. *Opuntia dillenii* is a cladode-type cactus that thrives in arid and semi-arid regions, requires minimal agricultural input, and is widely available in many parts of the world. The plant is known to contain a high pectin content, making it an attractive candidate for bio-based material development.[19] Moreover, the use of cactus-derived pectin offers multiple sustainability advantages, including biodegradability, non-toxicity, and the valorization of low-cost biomass that is often underutilized or discarded.

Although previous studies have investigated pectin extracted from various plant sources for environmental applications,[20,21] research focusing on *Opuntia dillenii*-derived pectin remains scarce. Existing studies on this cactus species have primarily concentrated on phytochemical extraction and biomedical aspects, with very limited exploration of its potential as a functional material for environmental remediation. To the best of our knowledge, no systematic study has yet reported the fabrication of a multi-component composite adsorbent based on *Opuntia dillenii* pectin combined with other natural polymers and porous additives for dye adsorption, nor has the adsorption mechanism, reusability, and structural stability of such composites been comprehensively evaluated.

The SPCA composite developed in this study holds several compelling advantages over conventional and emerging adsorbents. The primary feedstock – pectin extracted from *Opuntia dillenii* cladodes-is derived from a fast-growing, drought-tolerant cactus that requires minimal agricultural input and is widely available in tropical and semi-arid regions, constituting a virtually zero-cost and abundantly renewable raw material.[19] This approach directly parallels the philosophy of industrial waste valorization advocated in zeolite–activated carbon (Ze–AC) composites, where lithium–silicon-powder (LSP)-a solid by-product generated at approximately 10 tons per ton of lithium carbonate produced—was repurposed as the primary silica–alumina source to avoid resource waste and landfill disposal.[22] However, unlike LSP-derived Ze–AC, which requires acid pretreatment with hydrochloric acid, alkaline hydrothermal synthesis at 100 °C in NaOH solution, and multi-step washing procedures, the fabrication of SPCA proceeds entirely under mild aqueous conditions at ambient temperature *via* ionotropic gelation, without recourse to corrosive reagents, elevated temperatures, or pressurized reactors. The remaining components of SPCA – sodium alginate, chitosan, glycerol, and sodium bicarbonate-are either naturally occurring biopolymers or inexpensive commodity chemicals of low toxicity, further minimizing the overall material cost.[12,13] The environmental contrast becomes even more pronounced when SPCA is compared with metal–organic framework (MOF)-based adsorbents. Although MOFs exhibit outstanding porosity and tunability, their large-scale synthesis remains critically hampered by the use of toxic organic solvents such as DMF or DEF, corrosive metal precursors including metal nitrates and chlorides, and energy-intensive solvothermal conditions requiring pressurized reactors operating above the solvent boiling point.[23] In sharp contrast, SPCA was fabricated without any organic solvent, without environmentally hazardous metal precursors, and under ambient conditions that consume minimal energy, rendering its synthesis process inherently greener and more scalable. The use of sodium bicarbonate – a non-toxic, food-grade pore-forming agent – eliminates hazardous templating agents, while glutaraldehyde was employed at a minimal effective concentration of only 1 wt%, limiting crosslinker-associated toxicity and chemical waste.[24–26] Furthermore, the selection of air drying over freeze drying as the final processing step significantly reduces energy consumption while preserving satisfactory adsorption performance, an important consideration for large-scale deployment.[27] From an operational standpoint, the demonstrated reusability of SPCA over six consecutive adsorption–desorption cycles using ethanol – a relatively benign and readily recoverable solvent – substantially lowers the long-term operational cost per unit of dye removed, a metric of critical importance in practical wastewater treatment.[28] This regeneration stability is comparable to that reported for Ze–AC composites, which retained appreciable adsorption capacity for both NH_4^+-N and methylene blue across multiple cycles, while avoiding the high-temperature activation and inorganic regenerant protocols typically required for conventional carbon- and zeolite-based systems.[29]

In this context, the present study aims to bridge this research gap by developing a novel bio-based composite adsorbent derived from *Opuntia dillenii* pectin for the efficient removal of methyl orange (MO), a representative and widely used azo dye, from aqueous solutions. To the best of our knowledge, the integration of *Opuntia dillenii*-derived pectin with alginate, chitosan, and activated carbon through a dual ionic–covalent crosslinking strategy has not been previously reported for dye adsorption applications. Specifically, this work focuses on (i) the rational design and green synthesis of a multi-component composite using cactus-derived pectin, complementary biopolymers, and eco-friendly additives; (ii) comprehensive physicochemical characterization to elucidate the structural, thermal, and morphological properties of the composite; (iii) systematic investigation of adsorption performance, kinetics, and isotherm behavior toward MO; and (iv) evaluation of the regenerability and reusability of the composite over multiple adsorption–desorption cycles. By converting underutilized cactus biomass into a functional, reusable adsorbent, this study offers a sustainable approach to azo dye wastewater treatment while advancing biomass valorization and circular bio-based material development. Combined with a solvent-free, mild synthesis process, low chemical consumption, and multi-cycle reusability, SPCA emerges as a cost-effective and environmentally friendly material that meets both sustainability and economic requirements, in alignment with green chemistry and circular economy principles.

2. Materials and methods

2.1. Materials

Pectin was isolated from *Opuntia dillenii* using the following method: fresh *Opuntia dillenii* cladodes were collected in Lâm Đồng province (Vietnam), washed thoroughly, dried at 60 °C to constant weight, and ground into a fine powder. The cactus powder was mixed with an oxalic acid solution at a ratio of 1 : 30 (w/v), adjusted to pH 4.0, and heated at 100 °C for 1 h. Continuous stirring was applied during heating to ensure uniform extraction. After extraction, the mixture was cooled to room temperature and filtered through a cloth filter bag to remove solid residues. The filtrate was subsequently centrifuged to eliminate any remaining insoluble materials. The supernatant was then precipitated with 90% ethanol at an extract-to-ethanol ratio of 1 : 4 (v/v), followed by filtration and washing with 70% ethanol. The obtained pectin was dried at 60 °C for approximately 4 h, finely ground, and stored in glass containers for subsequent use.

Sodium alginate (Alg, $C_6H_7O_6Na$, purity ≥99%, analytical grade) was supplied as a brown powder by Tianjin Fuchen (China). Chitosan (average molecular weight ≈ 150 000 g mol^{-1}, degree of deacetylation ≥85%, purity ≥95%), sodium bicarbonate (purity ≥99%), activated carbon and methyl orange were obtained from Xilong (China). Glutaraldehyde solution (25 wt%, purity ≥98%) was purchased from Sigma-Aldrich (USA). Methyl orange (MO, purity ≥99%) used in adsorption experiments was supplied by Nanjing Reagent (China). Double-distilled water was used throughout all experiments, unless otherwise specified. Unless otherwise stated, all chemicals were of analytical grade and were used as received without further purification.

2.2. Preparation of composite materials (SPCA materials)

The detailed preparation procedure and the sequential fabrication steps of the SPCA composite beads are schematically illustrated in Fig. 1. First, sodium alginate and *Opuntia dillenii*-derived pectin were completely dissolved in double-distilled water under magnetic stirring for 1 h to obtain a homogeneous polymer solution. Subsequently, glycerol was added as a plasticizer, and the mixture was continuously stirred for an additional 1 h to improve chain flexibility and uniformity. Thereafter, sodium bicarbonate (as a pore-forming agent), chitosan, and activated carbon were sequentially introduced into the polymer matrix, followed by continuous stirring for 24 h to ensure complete dispersion and the formation of a homogeneous composite precursor solution. The resulting mixture was then slowly dropped into a 4 wt% zinc acetate (ZnAc) solution using a syringe under gentle stirring. This ionotropic gelation process was maintained for 1 h to promote bead formation, enhance hydrogel stability, and ensure complete structural development. The obtained hydrogel beads were repeatedly washed with double-distilled water to remove unreacted species and residual salts. Subsequently, the beads were immersed in a 1 wt% glutaraldehyde solution for 2 h to chemically crosslink the polymer chains and stabilize the composite structure. After crosslinking, the beads were thoroughly rinsed with double-distilled water, briefly soaked in a 1 wt% acetic acid solution for 15 min to neutralize excess crosslinker and improve surface properties, and then washed again to remove residual acid. Finally, the beads were immersed in 96% ethanol to facilitate

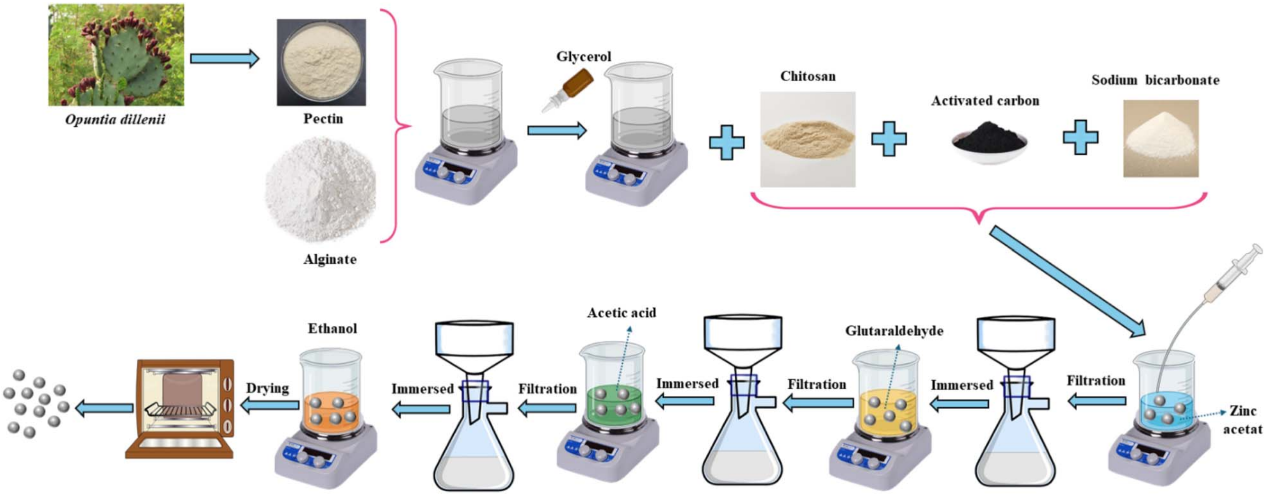

Fig. 1 Schematic representation of the stepwise fabrication process of SPCA composite beads derived from *Opuntia dillenii* biomass.

solvent exchange prior to drying and were vacuum-dried at −0.1 MPa and 60 °C for 2 h to obtain the final dried SPCA composite beads.

2.3. Characterization of composites

The mechanical stability of the hydrogel beads was evaluated using a rotary shaking test. Briefly, a total of 30 hydrogel beads were immersed in 100 mL of deionized water and subjected to continuous agitation at 180 rpm at room temperature. After 24 h of shaking, the beads were collected, dried to a constant weight, and weighed. The mass loss was calculated to quantify the extent of material dissolution during the mechanical agitation process. A lower amount of dissolved material corresponds to higher mechanical integrity and structural stability of the hydrogel beads under dynamic conditions.

$$\text{Mass loss}(\%) = \frac{W_0 - W_t}{W_0} \times 100\% \tag{1}$$

where W_0: initial mass of the particle (g) and W_t: mass of the particle after drying (g).

The swelling behavior of the prepared material was systematically investigated to evaluate its structural stability and water uptake capacity under different pH environments. Briefly, 0.5 g of the dried sample was accurately weighed and immersed in 50 mL of either 0.1 M HCl solution or phosphate-buffered saline (PBS, 0.1 M, pH 7.4). The suspensions were continuously agitated at a stirring speed of 200 rpm at room temperature to ensure uniform contact between the material and the swelling media. The samples were periodically removed from the solution at predetermined time intervals, gently blotted with filter paper to eliminate excess surface liquid, and weighed. The swelling process was monitored until noticeable morphological changes, such as cracking, fragmentation, or structural collapse of the particles, were observed, indicating the limit of structural integrity under the tested conditions. The swelling ratio (SR) was calculated according to the following equation:[30]

$$\text{Swelling ratio}(\%) = \frac{W_t - W_0}{W_0} \times 100\% \tag{2}$$

where W_t (g) is the mass of the material at swelling equilibrium or at a given time t, and W_0 (g) is the initial dry weight of the sample.

Fourier transform infrared (FTIR) spectroscopy was conducted to identify the surface functional groups of the composites before and after MO adsorption. The spectra were recorded in the wavenumber range of 400–4000 cm^{-1} using a Bruker Tensor 27 spectrometer. The crystalline structure of the composites was analyzed by X-ray diffraction (XRD) using a Bruker D8 Advance diffractometer with Cu Kα radiation. The XRD patterns were recorded over an appropriate 2θ range, and phase identification was performed based on the diffraction angles and peak positions corresponding to the crystalline and amorphous components of the materials. Thermogravimetric analysis (TGA) was performed on a Mettler Toledo thermogravimetric analyzer to assess the thermal stability and decomposition behavior of the composites. The measurements were carried out from room temperature to 600 °C at a heating rate of 10 °C min^{-1} under a nitrogen flow. Thermal properties of the composites were evaluated by differential scanning calorimetry (DSC). Approximately 10 mg of sample was placed in an aluminum crucible and heated from 25 to 300 °C at a heating rate of 10 °C min^{-1} under a nitrogen atmosphere using a differential scanning calorimeter. The specific surface area and pore size distribution of the composites were determined by nitrogen adsorption–desorption measurements using the Brunauer–Emmett–Teller (BET) method. The morphology and microstructural features of the composite particles were examined using scanning electron microscopy (SEM, JEOL JSM-IT200).

2.4. Decolorization of MO

Adsorption experiments were performed using material samples prepared under the optimal conditions identified in Section 2.2. A predetermined mass of the adsorbent was accurately weighed and added to beakers containing 50 mL of MO aqueous solutions with different initial pH values. The adsorption process was carried out at room temperature for a fixed contact time to ensure equilibrium conditions. After adsorption, the residual concentration of MO in solution was determined using UV-visible spectrophotometry at the maximum absorption wavelength ($\lambda_{\max} = 464$ nm). All experiments were conducted in triplicate to ensure reproducibility, and the average values along with standard deviations were calculated. The removal efficiency (%) and the equilibrium adsorption capacity (q_e, mg g^{-1}) of MO were calculated using eqn (3) and (4), respectively, based on the initial and equilibrium concentrations of the dye in solution.[31]

$$\text{Removal efficency (\%)} = \frac{C_0 - C_e}{C_0} \times 100 \tag{3}$$

$$q_e(\text{mg}\cdot\text{g}^{-1}) = \frac{(C_0 - C_e) \times V}{m} \tag{4}$$

where C_0 (mg L^{-1}) represents the initial MO concentration, C_e (mg L^{-1}) denotes the equilibrium concentration of MO in solution, V (L) refers to the volume of the dye solution, and m (g) corresponds to the dry mass of the adsorbent.

2.5. Adsorption isotherm studies

To elucidate the adsorption behavior and surface characteristics of the prepared composite toward MO, the equilibrium adsorption data were analyzed using the Langmuir, Freundlich, and Temkin isotherm models.

The Langmuir isotherm model assumes monolayer adsorption on a structurally homogeneous surface with a finite number of identical adsorption sites, where each site accommodates only one adsorbate molecule and no interactions occur between adjacent adsorbed species. The linearized Langmuir equation is expressed as follows:[32]

$$\frac{C_e}{q_e} = \frac{1}{q_{\max}\cdot K_L} + \frac{C_e}{q_{\max}} \tag{5}$$

where q_e (mg g^{-1}) is the adsorption capacity at equilibrium, $q_{\max}$ (mg g^{-1}) represents the maximum monolayer adsorption capacity, C_e (mg L^{-1}) is the equilibrium concentration of the adsorbate in solution, and K_L (L mg^{-1}) is the Langmuir adsorption constant related to the affinity of the binding sites.

The Freundlich isotherm model is an empirical equation that describes adsorption on heterogeneous surfaces with non-uniform distribution of adsorption energies and the possibility of multilayer adsorption. The linearized Freundlich equation is given by:[32]

$$\ln(q_e) = \ln(K_F) + \frac{1}{n}\ln(C_e) \tag{6}$$

where K_F ((mg g^{-1}) (L mg^{-1})$^{1/n}$) is the Freundlich constant indicative of adsorption capacity, and n is the heterogeneity factor related to adsorption intensity. Values of $1/n$ between 0 and 1 indicate favorable adsorption conditions.

The Temkin isotherm model considers adsorbent–adsorbate interactions and assumes that the heat of adsorption of all molecules in the layer decreases linearly with surface coverage due to these interactions. The linear form of the Temkin equation is expressed as:[32]

$$q_e = B\ln(A_t) + B\ln(C_e) \tag{7}$$

In which R (8.314 J mol^{-1} K^{-1}) is the universal gas constant, T (K) is the absolute temperature, and b (J mol^{-1}) represents the Temkin isotherm constant associated with adsorption energy.

2.6. Adsorption kinetics models

To elucidate the adsorption mechanism and rate-controlling steps governing MO uptake onto the prepared composite, the experimental kinetic data were analyzed using the pseudo-first-order (PFO), pseudo-second-order (PSO), intraparticle diffusion, and Elovich kinetic models.

The pseudo-first-order (PFO) kinetic model is commonly applied to adsorption systems in which the rate of occupation of adsorption sites is proportional to the number of unoccupied sites, and mass transfer is predominantly governed by surface adsorption rather than intraparticle diffusion. The linearized form of the PFO model is expressed as follows:[32]

$$\log(q_e - q_t) = \log q_e - \frac{k_1}{2303} \times t \tag{8}$$

where k_1 (h^{-1}) is the pseudo-first-order rate constant, q_e (mg g^{-1}) denotes the adsorption capacity at equilibrium, q_t (mg g^{-1}) represents the adsorption capacity at time t, and t (h) is the contact time.

The pseudo-second-order (PSO) kinetic model is widely used to describe adsorption processes controlled by chemisorption mechanisms involving valence forces through electron sharing or exchange between the adsorbent and adsorbate. The linear form of the PSO model is given by:[32]

$$\frac{t}{q_t} = \frac{1}{k_2 {q_e}^2} + \frac{t}{q_e} \tag{9}$$

where k_2 (g mg^{-1} h^{-1}) is the pseudo-second-order rate constant.

The intraparticle diffusion model, proposed by Weber and Morris, is employed to evaluate whether pore diffusion is the rate-limiting step in the adsorption process. This model is described by the following equation:[33]

$$q_t = k_p\cdot t^{0,5} + C \tag{10}$$

where k_p (mg g^{-1} h$^{-1/2}$) is the intraparticle diffusion rate constant, and C (mg g^{-1}) is the intercept associated with the thickness of the boundary layer. A larger value of C indicates a greater contribution of surface adsorption or film diffusion to the overall adsorption process.

The Elovich kinetic model is applicable to heterogeneous adsorption systems and is often used to describe chemisorption processes involving surface and intraparticle diffusion simultaneously. The simplified linear form of the Elovich equation is expressed as follows:[33]

$$q_t = \frac{1}{\beta}\ln(\alpha\beta) + \frac{1}{\beta}\ln(t) \tag{11}$$

where α (mg g^{-1} h^{-1}) represents the initial adsorption rate, and β (g mg^{-1}) is the Elovich constant related to the extent of surface coverage and activation energy for chemisorption.

2.7. Desorption and regeneration studies

Following the adsorption of MO under the optimized experimental conditions, the adsorbent beads were gently separated from the solution and thoroughly rinsed with distilled water to remove physically bound dye molecules. The beads were then transferred into various desorbing media, including 0.1 N NaOH, 0.1 N HCl, 96% methanol, 96% ethanol, and 0.05 M $NaHCO_3$ solutions, and magnetically stirred for 2 h at room temperature to facilitate dye desorption. After desorption, the beads were repeatedly washed with distilled water until neutral pH was attained, dried to a constant weight, and subsequently reused in fresh MO solutions (50 mL) under the same initial adsorption conditions. The adsorption efficiency after each cycle was determined to evaluate the reusability of the adsorbent. The desorbing agent exhibiting the highest desorption efficiency and minimal structural degradation was selected for subsequent adsorption–desorption-re-adsorption cycles. The regeneration process was continued until the adsorbent exhibited a pronounced decline in adsorption capacity or structural instability, indicating the practical lifetime of the composite material.

3. Results and discussion

3.1. Effect of conditions for composite synthesis on the adsorption performance

3.1.1. Effect of drying methods on the composite beads. The drying strategy plays a pivotal role in dictating the internal pore architecture, surface accessibility, and mass-transfer resistance of the composite beads, thereby exerting a decisive influence on their adsorption behavior toward MO (Fig. 2A). As clearly evidenced by the experimental data, beads in the wet state exhibited extremely poor adsorption performance, with an adsorption efficiency of only 24.60 ± 1.70% and a corresponding adsorption capacity of 1.23 ± 0.08 mg g^{-1}. This markedly low uptake can be ascribed to the substantial amount of retained water occupying the internal pore space, which effectively blocks diffusion pathways and limits access to active adsorption sites. Under such conditions, MO transport is predominantly governed by external film diffusion, while intraparticle diffusion is severely suppressed, resulting in inefficient utilization of the internal surface area. Upon air drying, a pronounced enhancement in adsorption performance was observed. The air-dried beads (ADB) achieved an adsorption efficiency of 85.09 ± 1.29% and an adsorption capacity of 4.25 ± 0.06 mg g^{-1}, corresponding to an approximately 3.5-fold increase in capacity relative to wet beads. This substantial improvement indicates that solvent evaporation during air drying partially opens the internal pore structure and exposes a larger fraction of functional adsorption sites, while maintaining sufficient mechanical integrity of the beads. Although some degree of pore shrinkage is inevitable due to capillary stresses during evaporation, the resulting porous network remains adequately accessible to facilitate effective intraparticle diffusion of MO molecules. Freeze-dried beads exhibited the highest adsorption performance, with an adsorption efficiency of 94.85 ± 1.81%, which is approximately 9.76% higher than that of air-dried beads. This superior performance can be attributed to the formation of a highly interconnected and hierarchical porous structure generated through ice-crystal templating and subsequent sublimation, which minimizes mass-transfer resistance and maximizes the availability of adsorption sites.[27] However, the incremental gain in adsorption efficiency compared to air-dried beads is relatively modest when weighed against the significantly higher energy consumption, prolonged processing time, and increased operational cost associated with freeze drying. From a practical and sustainability-oriented perspective, air drying emerges as the most rational and application-relevant strategy. It offers a favorable balance between adsorption performance, process simplicity, economic viability, and scalability, while avoiding the excessive energy demand inherent to freeze drying. Therefore, despite the slightly lower adsorption efficiency compared to freeze-dried beads, air-dried beads were selected as the optimal drying condition for subsequent optimization and mechanistic investigations.

3.1.2. Effect of sodium alginate/pectin ratio. The sodium alginate/pectin (SP) ratio plays a decisive role in regulating polymer network formation, ionic crosslinking density, and the spatial distribution of adsorption-active functional groups within the composite beads, thereby directly governing their adsorption performance toward MO (Fig. 2B). At a low alginate content (SP = 2/1), the adsorption efficiency was limited to 79.75 ± 0.96%, indicating that the alginate fraction was insufficient to establish a mechanically robust and uniformly crosslinked polymer network. As a result, the composite matrix likely exhibits poor structural coherence, heterogeneous pore morphology, and limited pore interconnectivity, which collectively impede effective intraparticle diffusion and restrict access to internal adsorption sites. Increasing the SP ratio to 3/1 and 4/1 led to a substantial enhancement in adsorption efficiency, reaching 85.09 ± 1.29% and 86.40 ± 0.35%, respectively, with corresponding adsorption capacities of 4.25–4.31 mg g^{-1}. This improvement reflects the emergence of optimal synergistic interactions between sodium alginate and *Opuntia dillenii* pectin, resulting in a well-integrated polymer network with balanced crosslinking density and a highly accessible porous architecture. Within this compositional window, alginate provides sufficient ionic crosslinking to ensure structural stability and resistance to deformation, while pectin contributes a high density of carboxyl functional groups that act as the primary adsorption sites. The combined effect promotes efficient electrostatic interactions between anionic MO molecules and protonated functional groups, alongside enhanced physical adsorption through pore filling and diffusion-driven transport. However, further increasing the alginate fraction to SP = 5/1 resulted in a noticeable decline in adsorption efficiency to

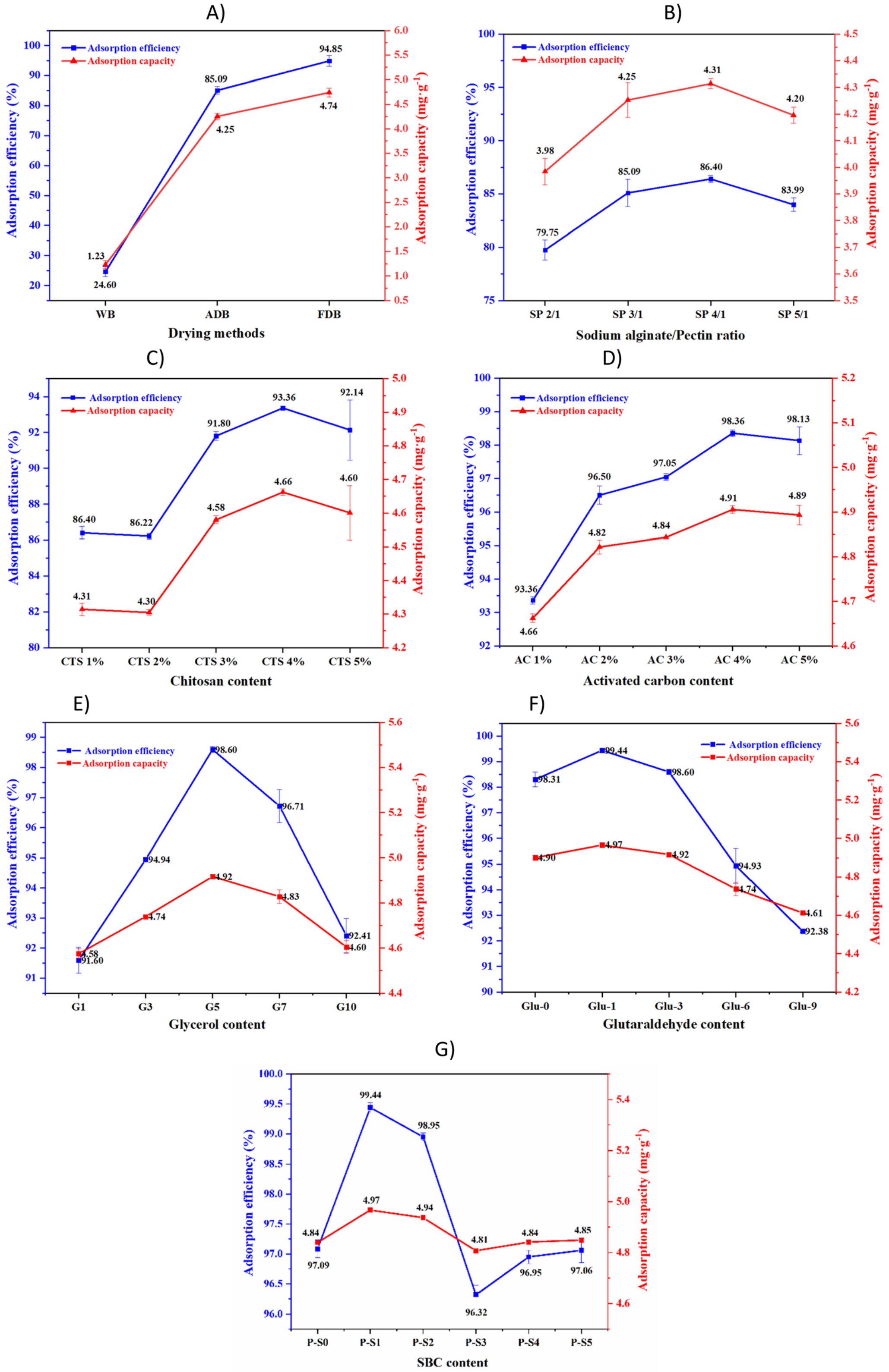

Fig. 2 Effect of drying methods (A) and composition material (B, C, D, E, F, and G) for the adsorption efficiency MO.

83.99% and a reduction in adsorption capacity to 4.20 mg g^{-1}. This deterioration can be attributed to the dilution of pectin-derived adsorption-active sites and excessive chain packing induced by the higher alginate content. The increased rigidity and compactness of the polymer network likely suppress pore accessibility and elevate mass-transfer resistance, thereby limiting dye diffusion into the internal structure and reducing effective site utilization. Overall, these findings underscore the pivotal role of pectin as the dominant adsorption-active component and highlight the necessity of compositional balance between alginate-induced structural integrity and pectin-derived functional group availability. Among the investigated formulations, an SP ratio of 4/1 provides the most favorable compromise between network stability, pore accessibility, and functional site density, ultimately yielding superior adsorption performance through synergistic polymer network design.

3.1.3. Effect of chitosan content. As illustrated in Fig. 2C, the incorporation of chitosan exerts a pronounced influence on the adsorption behavior of the composite beads. Increasing the CTS content from 1% to 4% resulted in a progressive enhancement in adsorption efficiency from 86.40 ± 0.35% to 93.36 ± 0.11%, accompanied by a corresponding increase in adsorption capacity from 4.31 ± 0.02 mg g^{-1} to 4.66 ± 0.01 mg g^{-1}. This improvement can be primarily attributed to the increased density of amino functional groups introduced by chitosan. Under the experimental conditions, these amino groups are predominantly protonated ($-NH_3^+$), enabling strong electrostatic attraction with the anionic sulfonate ($-SO_3^-$) groups of MO, thereby significantly enhancing dye uptake.[34] At the optimal CTS content of 4%, the composite matrix achieves an effective balance between functional group availability and pore accessibility. The abundance of $-NH_3^+$ groups maximizes electrostatic binding sites, while the polymer network remains sufficiently open to facilitate efficient intraparticle diffusion. Consequently, both adsorption efficiency and capacity reach their maximum values, indicating highly effective utilization of internal adsorption sites. However, further increasing the CTS content beyond 4% led to a decline in adsorption efficiency despite the higher overall polymer loading. This deterioration is attributed to excessive chitosan chains inducing increased solution viscosity during bead formation and promoting chain aggregation within the solidified matrix.[35] Such aggregation partially blocks pore channels and reduces pore interconnectivity, thereby increasing mass-transfer resistance and limiting MO diffusion into the internal structure. Under these conditions, the adsorption process transitions from being predominantly governed by functional group availability to being constrained by intraparticle diffusion and steric hindrance, resulting in reduced effective surface utilization. Overall, these findings demonstrate that chitosan plays a critical role as an adsorption-active component by providing cationic functional groups, but its content must be carefully optimized. A CTS loading of 4% represents the optimal composition, delivering the highest adsorption performance by simultaneously maximizing electrostatic interactions and preserving favorable mass-transfer characteristics within the composite beads.

3.1.4. Effect of activated carbon content. As shown in Fig. 2D, the incorporation of activated carbon (AC) exerts a substantial and systematic enhancement on the adsorption performance of the composite beads. Increasing the AC content from 1% to 4% resulted in a marked rise in adsorption efficiency from 93.36 ± 0.11% to 98.36 ± 0.10%, while the adsorption capacity increased correspondingly from 4.66 ± 0.01 mg g^{-1} to 4.91 ± 0.01 mg g^{-1}. This improvement is primarily attributed to the intrinsic characteristics of AC, namely its high specific surface area and well-developed microporous structure, which introduce abundant additional adsorption sites within the composite matrix.[29] Moreover, the graphitic domains of AC facilitate strong π–π interactions with the aromatic rings of MO, thereby reinforcing dye adsorption beyond electrostatic and hydrogen-bonding interactions provided by the biopolymer components. At an AC loading of 4%, an optimal synergistic architecture is achieved, in which AC particles are homogeneously dispersed within the polymer network, preserving pore connectivity and ensuring efficient mass transfer. This structural synergy is further supported by the pronounced mass increase after adsorption, indicating effective dye retention within both the polymeric and carbonaceous domains while maintaining high mechanical stability. In contrast, further increasing the AC content to 5% did not yield proportional performance gains. Although the adsorption capacity remained comparable (4.89 ± 0.02 mg g^{-1}), the adsorption efficiency slightly decreased to 98.14 ± 0.42%, accompanied by a notable reduction in mass increase after adsorption. This behavior suggests that excessive AC loading leads to partial agglomeration and disruption of the polymer matrix continuity, which diminishes effective surface utilization and compromises structural integrity. The resulting increase in interfacial defects and diffusion resistance limits the accessibility of adsorption sites, thereby reducing overall adsorption efficiency. Overall, these results demonstrate that activated carbon functions as a highly effective adsorption enhancer when incorporated at an optimal level. An AC content of 4% provides the most favorable balance between surface area augmentation, pore connectivity, and mechanical robustness, maximizing adsorption efficiency through the synergistic integration of microporous carbon domains within the biopolymer-based composite framework.

3.1.5. Effect of glycerol content. As illustrated in Fig. 2E, glycerol content plays a decisive role in regulating the adsorption behavior of the composite beads by modulating polymer chain mobility and pore evolution during drying. Increasing the glycerol concentration progressively enhanced adsorption performance, reaching a maximum adsorption efficiency of 98.60 ± 0.10% and an adsorption capacity of 4.92 ± 0.01 mg g^{-1} at an optimal glycerol content of 5%. At this concentration, glycerol acts as an effective green plasticizer, reducing intermolecular hydrogen bonding among polymer chains and increasing their flexibility.[36] This controlled plasticization facilitates uniform pore development, mitigates excessive shrinkage during solvent evaporation, and preserves an interconnected porous architecture with high surface accessibility. The optimized microstructure obtained at 5% glycerol promotes efficient intraparticle diffusion of MO molecules and maximizes the exposure of adsorption-active functional groups, thereby enhancing both adsorption efficiency and capacity. The balance between chain flexibility and structural integrity at this glycerol level is crucial for achieving high adsorption performance. However, further increasing the glycerol content beyond the optimal level resulted in a noticeable decline in adsorption efficiency (decreasing to approximately 92% at 10% glycerol). This deterioration can be attributed to excessive plasticization, which weakens intermolecular interactions and reduces crosslinking effectiveness within the polymer network.[37] As a consequence, the composite structure becomes mechanically less stable, increasing the likelihood of pore collapse, excessive swelling, or partial blocking of diffusion pathways. These structural defects reduce the effective surface area available for adsorption and elevate mass-transfer resistance, ultimately diminishing dye uptake. Overall, the non-monotonic dependence of adsorption performance on glycerol content highlights the critical importance of controlled plasticization. An optimal glycerol concentration of 5% provides the most favorable compromise between network flexibility, pore stability, and adsorption-site accessibility, underscoring glycerol's essential role in the rational design of high-performance, sustainable bio-based adsorbent composites.

3.1.6. Effect of glutaraldehyde concentration. As depicted in Fig. 2F, the glutaraldehyde concentration plays a pivotal role in regulating crosslinking density, pore architecture, and the accessibility of adsorption-active functional groups, thereby exerting a pronounced influence on the adsorption performance of the composite beads. At an optimal glutaraldehyde concentration of 1%, the material exhibited the highest adsorption efficiency of 99.44 ± 0.08%, indicating a well-balanced polymer network that combines sufficient mechanical stability with high functional group availability. At this crosslinker level, glutaraldehyde forms covalent linkages primarily with hydroxyl (–OH) and amino ($-NH_2$) groups on alginate, pectin, and chitosan chains, resulting in a stabilized three-dimensional network while preserving a significant fraction of accessible adsorption sites.[24–26] The moderately cross-linked structure maintains an open pore network that facilitates effective intraparticle diffusion of MO molecules and promotes strong electrostatic and hydrogen-bonding interactions during adsorption. In contrast, at lower glutaraldehyde concentrations, insufficient crosslinking leads to weak network cohesion and reduced mechanical integrity, making the beads more susceptible to structural deformation or partial dissolution during adsorption. Conversely, increasing the glutaraldehyde concentration beyond 1% induces over-crosslinking, which progressively reduces adsorption efficiency, declining to approximately 92% at 9% glutaraldehyde. Excessive crosslinking densifies the polymer matrix, causing pore shrinkage and elevated mass-transfer resistance. Moreover, the consumption and masking of surface-exposed –OH and $-NH_2$ groups by excessive covalent bonding significantly diminish the number of effective adsorption sites. These results clearly demonstrate that adsorption performance is governed by an optimal crosslinking regime rather than maximal crosslink density. Achieving a delicate balance between network stability and functional group accessibility is therefore essential for the rational design of high-performance, reusable bio-based adsorbents.

3.1.7. Effect of sodium bicarbonate content. Sodium bicarbonate (SBC) acts as a green and efficient pore-forming agent by generating CO_2 *in situ* upon exposure to acidic conditions, thereby playing a decisive role in tailoring the internal pore architecture of the composite beads (Fig. 2G). At an SBC content of 1%, the composite exhibited the highest adsorption efficiency of 99.44 ± 0.08% and a corresponding adsorption capacity of 4.97 ± 0.01 mg g^{-1}, accompanied by a moderate post-adsorption mass increase of 4.12 ± 0.69%. These results indicate the formation of an optimally developed hierarchical pore network, comprising interconnected micro- and mesopores, which markedly enhances capillary-driven dye uptake and facilitates rapid intraparticle diffusion of MO molecules the controlled evolution of CO_2 bubbles at this SBC level creates well-distributed voids throughout the polymer matrix without disrupting network integrity. This porous architecture not only increases the effective surface area but also reduces internal mass-transfer resistance, allowing MO molecules to penetrate deeply into the adsorbent and efficiently interact with adsorption-active functional groups *via* electrostatic attraction and hydrogen bonding. In contrast, further increasing the SBC content resulted in a gradual decline in adsorption performance, with adsorption efficiency decreasing to approximately 96% at 3% SBC.

Excessive CO_2 generation under these conditions likely induces rapid pore expansion and coalescence, leading to irregular pore morphology, partial pore collapse, and weakened mechanical stability of the beads. Such structural defects elevate diffusion resistance and limit the effective utilization of internal adsorption sites, thereby diminishing overall adsorption efficiency despite increased porosity. Collectively, these findings demonstrate that judicious control of SBC content is essential for effective pore engineering. When optimally dosed, sodium bicarbonate enables the green fabrication of mechanically robust, hierarchically porous composites with superior adsorption performance, highlighting its suitability for sustainable adsorbent design and large-scale environmental applications.

3.2. Characterization of the composite

The mechanical stability of the SPCA composite beads was evaluated through mass-loss analysis after prolonged agitation in aqueous media. The material exhibited a low mass loss of 2.06 ± 0.07% ($n = 3$), indicating excellent structural integrity and resistance to dissolution or erosion. Such a minimal mass loss reflects the effectiveness of the crosslinked polymer network in maintaining bead cohesion under dynamic conditions, which is a critical prerequisite for repeated adsorption–desorption cycles in practical wastewater treatment applications.

The swelling behavior of SPCA beads was systematically investigated in 0.1 M HCl to simulate acidic environments commonly encountered in dye-containing wastewater. As summarized in Fig. 3, the swelling process followed a characteristic three-stage kinetic profile, reflecting the progressive interaction between the polymer network and the surrounding medium. During the initial stage (0–1.5 h), the beads exhibited rapid swelling, driven by the immediate wetting of the surface and fast penetration of water molecules into the interconnected porous structure. This phase is governed primarily by capillary

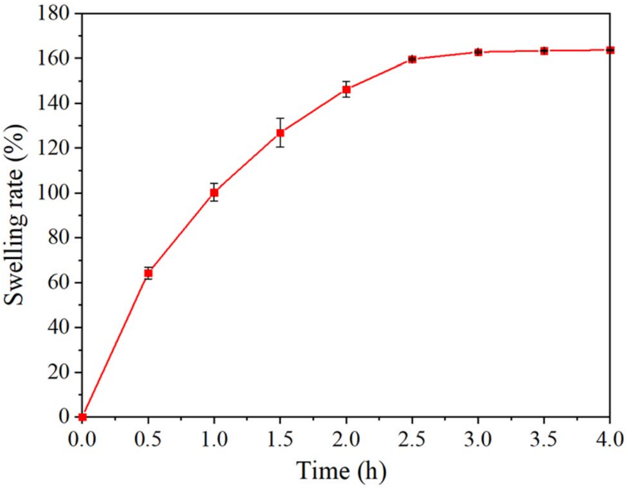

Fig. 3 Temporal swelling rate of SPCA in 0.1 M HCl solution.

forces and osmotic pressure gradients, allowing water to diffuse readily into accessible voids and hydrophilic domains. In the intermediate stage (1.5–2.5 h), the swelling rate gradually decreased as internal pores became increasingly saturated. At 2.5 h, the swelling degree reached 159.58%, indicating that the polymer chains had undergone substantial relaxation and expansion. At this stage, resistance from the crosslinked network counterbalanced further water uptake, signaling an approach toward equilibrium swelling. In the final stage (3–4 h), the system attained a stable swelling equilibrium, with swelling ratios fluctuating narrowly between 162.79% and 163.67%, confirming full saturation of the polymer matrix. The stable plateau suggests that the network structure effectively accommodates water without undergoing structural damage or dissolution. The pronounced swelling capacity of SPCA in acidic media can be attributed to its highly hydrophilic polymer framework, composed of sodium alginate and pectin rich in hydroxyl (–OH) and carboxyl (–COOH) groups. Under acidic conditions, partial protonation of carboxyl groups reduces electrostatic repulsion while preserving hydrogen bonding with water molecules, thereby promoting controlled swelling without compromising network stability.[38,39] In contrast, when immersed in phosphate-buffered saline (PBS, 0.1 M, pH 7.4), the SPCA beads underwent complete dissolution.

PBS represents a salt-rich, mildly alkaline environment in which ionic strength is sufficiently high to disrupt electrostatic interactions and hydrogen bonding within the polymer matrix. Specifically, phosphate ions and sodium ions effectively screen ionic crosslinks and weaken intermolecular associations between polymer chains, leading to the breakdown of the crosslinked network and subsequent bead disintegration.[30,40] Overall, these results demonstrate that SPCA beads exhibit excellent mechanical stability and controlled swelling behavior in acidic environments, which is advantageous for the adsorption of anionic dyes such as methyl orange. At the same time, their susceptibility to dissolution in alkaline, high-ionic-strength media highlights a stimuli-responsive behavior, which may be strategically exploited for material regeneration or environmentally benign disposal after use.

The FT-IR spectra provide compelling evidence for the successful integration of alginate, *Opuntia dillenii* pectin, chitosan, and activated carbon into a chemically interactive composite rather than a simple physical mixture (Fig. 4A). For sodium alginate and cactus pectin, the characteristic broad absorption band in the range of 3400–3440 cm^{-1} is attributed to the stretching vibration of hydroxyl groups (–OH), arising from abundant polysaccharide chains and adsorbed water molecules.[41,42] In the SPCA spectrum, this band becomes noticeably broader and slightly shifted, consistent with observations on *Opuntia ficus-indica*-based adsorbents where abundant hydroxyl groups from pectin, cellulose, and mucilage give rise to a broad, unresolved O–H envelope that broadens further upon composite formation due to the formation of an extensive hydrogen-bonding network among –OH groups of alginate, pectin, glycerol, and chitosan.[43,44] Such hydrogen bonding contributes significantly to the structural cohesion and hydrophilicity of the composite. The absorption bands observed at

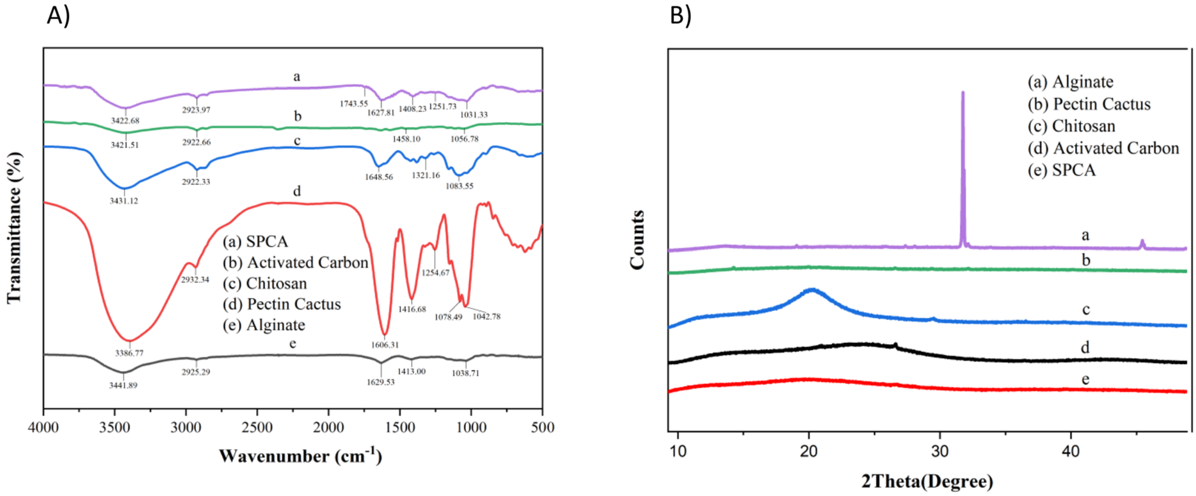

Fig. 4 FT-IR spectra (A) and X-ray diffraction (B) of SPCA and corresponding materials.

$\sim$2923 cm^{-1} correspond to asymmetric C–H stretching vibrations of aliphatic –CH_2 and –CH_3 groups,[45] which are common to all polysaccharide components and glycerol. The persistence of these bands in SPCA confirms that the polymer backbones remain chemically intact during composite fabrication. A key feature of alginate and pectin is the presence of carboxylate groups. In the spectra of pure alginate and pectin, the asymmetric and symmetric stretching vibrations of –COO^- groups appear at approximately 1629–1631 cm^{-1} and 1408–1416 cm^{-1}, respectively.[46,47] In the SPCA composite, the asymmetric –COO^- band shifts to $\sim$1627 cm^{-1}, accompanied by changes in intensity and band shape. This shift provides strong evidence for ionic coordination between carboxylate groups and Zn^{2+} ions, leading to the formation of the classical "egg-box" structure.[48] Such coordination restricts polymer chain mobility and stabilizes the three-dimensional network, which is essential for mechanical robustness and reusability during adsorption–desorption cycles. Chitosan incorporation is evidenced by the presence of an absorption band at $\sim$1648 cm^{-1}, assigned to the amide I vibration (C=O stretching).[49] Compared to pure chitosan, this band in SPCA exhibits slight shifting and broadening, suggesting strong intermolecular interactions between chitosan amino groups (–NH^2/–NH_3^+) and the carboxylate groups of alginate and pectin. Although the –OH and N–H stretching vibrations of chitosan in the 3000–3600 cm^{-1} region are well known to overlap and produce a broad, unresolved absorption band—a spectroscopic limitation inherent to chitosan-containing systems—the successful incorporation of chitosan into the SPCA composite was unambiguously confirmed by the characteristic amide I band at $\sim$1648 cm^{-1} and its discernible shift and broadening in the composite spectrum, which are attributable to strong intermolecular interactions between chitosan amino groups and the carboxylate moieties of alginate and pectin. These interactions are further reinforced by hydrogen bonding and, under acidic conditions, electrostatic attraction, which collectively enhance the density of adsorption-active sites for anionic dye molecules. The intense band appearing at $\sim$1031–1056 cm^{-1} in the SPCA spectrum is attributed to C–O–C and C–O stretching vibrations characteristic of polysaccharide glycosidic linkages, confirmed also by the porous carbon FTIR fingerprint region documented for potassium-citrate-derived activated carbons[50] and for cellulose-chitosan-alginate composite beads.[51,52] The presence and intensity of this band confirm that the polysaccharide framework is preserved while actively participating in network formation. Additionally, weak and broadened bands in the region of $\sim$1500–1600 cm^{-1} and $\sim$1200–1000 cm^{-1} can be associated with surface functional groups of activated carbon, including aromatic C=C, C–O, and C=O vibrations.[53] Although these bands are relatively subtle due to the carbonaceous nature of activated carbon, their presence indicates successful incorporation and surface exposure, which is crucial for π–π interactions with the aromatic rings of methyl orange.[54] Overall, the FT-IR analysis demonstrates that SPCA is stabilized through a combination of ionic crosslinking (Zn^{2+}–COO^-), hydrogen bonding, and secondary interactions involving chitosan and activated carbon.

These synergistic interactions generate a chemically integrated, multifunctional adsorption network with abundant accessible functional groups, providing a strong structural basis for the high adsorption efficiency and reusability observed in subsequent adsorption studies.

The crystalline structures of alginate, cactus pectin, chitosan, activated carbon, and the SPCA composite were investigated by X-ray diffraction (XRD), as shown in Fig. 4B. The diffractograms reveal distinct structural characteristics of the individual components and provide clear evidence for the formation of an integrated composite with reduced crystallinity. Pure alginate (curve a) exhibits a sharp diffraction peak at $2\theta \approx 29.4°$, which is characteristic of its semi-crystalline nature and is commonly attributed to the ordered arrangement of polymer chains stabilized by inter- and intramolecular hydrogen bonding.[55] The high intensity and narrow width of this peak indicate a relatively high degree of structural ordering within the alginate matrix. Cactus pectin (curve b), in contrast, displays a predominantly amorphous pattern, characterized by a broad and low-intensity halo centered around $2\theta \approx$ 20–22°.[55] This broad diffraction feature reflects the disordered arrangement of pectin chains, which is typical for highly branched polysaccharides containing abundant galacturonic acid units and flexible side chains. Chitosan (curve c) shows a broad diffraction peak centered at $2\theta \approx$ 19.8–20.5°, corresponding to the (110) crystalline plane. The broadness of this peak suggests a semi-crystalline structure with limited long-range order, arising from partial crystallization induced by hydrogen bonding between –OH and –NH_2 groups along the chitosan backbone.[56] Activated carbon (curve d) exhibits a largely amorphous diffraction pattern, with a very broad and weak peak around $2\theta \approx$ 26–26.5°, which is associated with the (002) plane of turbostratic carbon.[57] The absence of sharp diffraction peaks confirms the disordered, non-graphitic structure of activated carbon, which is advantageous for adsorption due to its high surface defect density and porosity. Notably, the SPCA composite (curve e) presents a markedly different diffraction profile compared to the individual components. The sharp crystalline peak of alginate at $\sim$29.4° disappears completely, while the broad polysaccharide-related peaks around 20–22° become significantly weakened and broadened. This pronounced reduction in peak intensity and increase in peak width indicate a substantial decrease in crystallinity, confirming that strong intermolecular interactions occur during composite formation. The suppression of crystalline features in SPCA can be attributed to the synergistic effects of ionic crosslinking between Zn^{2+} ions and carboxylate groups (–COO^-) of alginate and pectin, electrostatic interactions between protonated chitosan (–NH_3^+) and carboxylate groups, and extensive hydrogen bonding among all polysaccharide components. These interactions disrupt the regular packing of polymer chains, thereby preventing recrystallization and promoting the formation of an amorphous three-dimensional network. From an application perspective, the reduced crystallinity of SPCA is highly beneficial for adsorption processes. Amorphous structures provide greater chain mobility, higher accessibility of functional groups, and increased diffusion pathways for

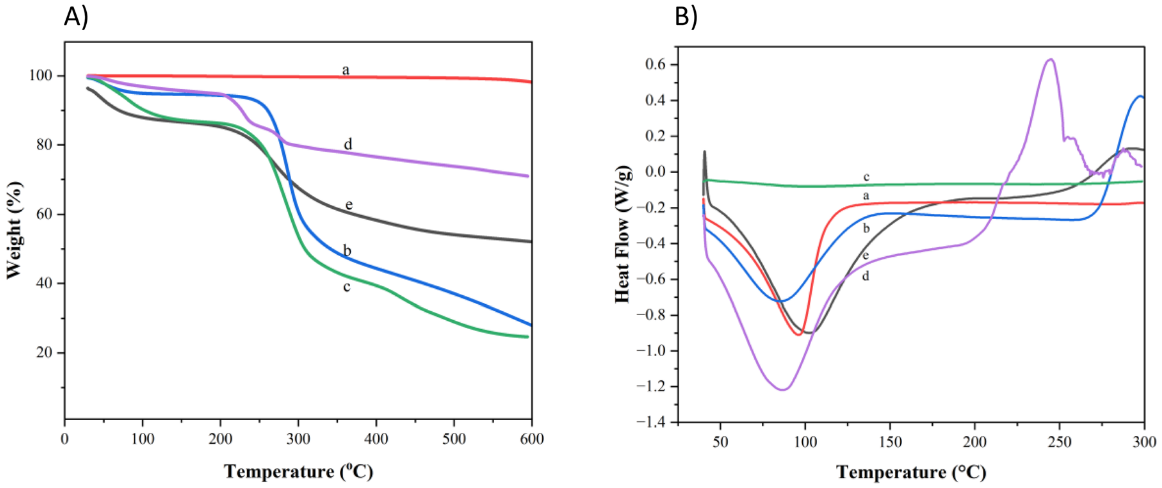

Fig. 5 Thermogravimetric analysis (TGA) (A) and differential scanning calorimetry (DSC) (B) of SPCA and related materias: (a) activated carbon, (b) chitosan, (c) pectin cactus, and (d) alginate.

adsorbate molecules, all of which contribute directly to enhanced dye uptake—consistent with the superior methylene blue removal capacity reported for amorphous, porous cactus-based adsorbents relative to their more crystalline counterparts.[43,44] Consequently, the XRD results strongly support the enhanced adsorption performance observed for SPCA, particularly toward organic dye molecules such as methyl orange.

The thermal behavior of the pristine polymers and the SPCA composite was systematically elucidated by the combined analysis of thermogravimetric analysis (TGA) and differential scanning calorimetry (DSC), providing complementary insights into mass loss phenomena, phase transitions, and polymer chain dynamics.

As shown in Fig. 5A, the thermal decomposition of pectin, chitosan, sodium alginate, and SPCA can be divided into three characteristic stages. The first stage (150–300 °C) corresponds to the initial thermal degradation of labile functional groups, dehydration of bound water, and cleavage of weak intermolecular interactions. In this temperature range, the pristine polysaccharides exhibit noticeable weight loss, whereas SPCA shows a delayed onset of degradation, indicating improved resistance to thermal activation. This observation is consistent with the DSC results (Fig. 5B), where sodium alginate and pectin display endothermic transitions at 100–150 °C and chitosan at 150–200 °C,[58,59] attributed to polymer relaxation and partial disruption of hydrogen bonding. In contrast, SPCA does not exhibit sharp transitions in this region, reflecting suppressed segmental mobility due to effective crosslinking. The second stage (300–500 °C) represents the main decomposition region, involving backbone scission of polysaccharide chains and extensive depolymerization.[60] In this stage, the individual raw materials undergo rapid and severe mass loss, while SPCA maintains a significantly lower weight loss of only ∼30–40%, demonstrating superior thermal stability. Correspondingly, the DSC curve of SPCA shows a broad and smooth endothermic behavior extending up to approximately 250 °C, rather than the sharp thermal events observed for the pristine polymers. This broadened transition reflects a highly integrated polymer network in which thermal energy is dissipated over a wide temperature range, delaying catastrophic chain breakdown. The enhanced thermal resistance of SPCA in this regime can be attributed to the dual crosslinking mechanism. Ionic coordination between Zn^{2+} ions and carboxylate groups of alginate and pectin (egg-box structure), together with covalent crosslinking between glutaraldehyde and chitosan amino groups, significantly restricts polymer chain motion.[61] As a result, higher thermal energy is required to initiate backbone decomposition, effectively extending the primary decomposition window to approximately 200–400 °C. In the final high-temperature stage (>500 °C), SPCA retains a substantial residual mass (20–25%), whereas the pristine polysaccharides are almost completely decomposed. This residual mass is associated with the formation of a stable carbonaceous structure reinforced by activated carbon.[29] The DSC data further support this interpretation, as the strong exothermic peak observed for activated carbon around 250–270 °C becomes attenuated and broadened in the SPCA composite, indicating strong interfacial interactions and homogeneous dispersion within the polymer matrix. Overall, the combined TGA-DSC analysis clearly demonstrates that the synergistic incorporation of polysaccharides, activated carbon, and dual crosslinking agents results in a thermally robust composite. The delayed decomposition onset, reduced mass loss, broadened thermal transitions, and increased char yield collectively confirm that SPCA possesses enhanced thermal stability and structural durability, which are critical for repeated adsorption–desorption cycles and long-term application in wastewater treatment.

The textural properties of SPCA before and after MO adsorption were systematically evaluated using N_2 adsorption–desorption measurements (Fig. 6) and the corresponding BET/BJH parameters summarized in Table S1. Prior to adsorption, SPCA exhibits a relatively high BET specific surface area of 255.88 $m^2\ g^{-1}$, confirming the presence of a well-developed porous framework favorable for adsorption processes. After

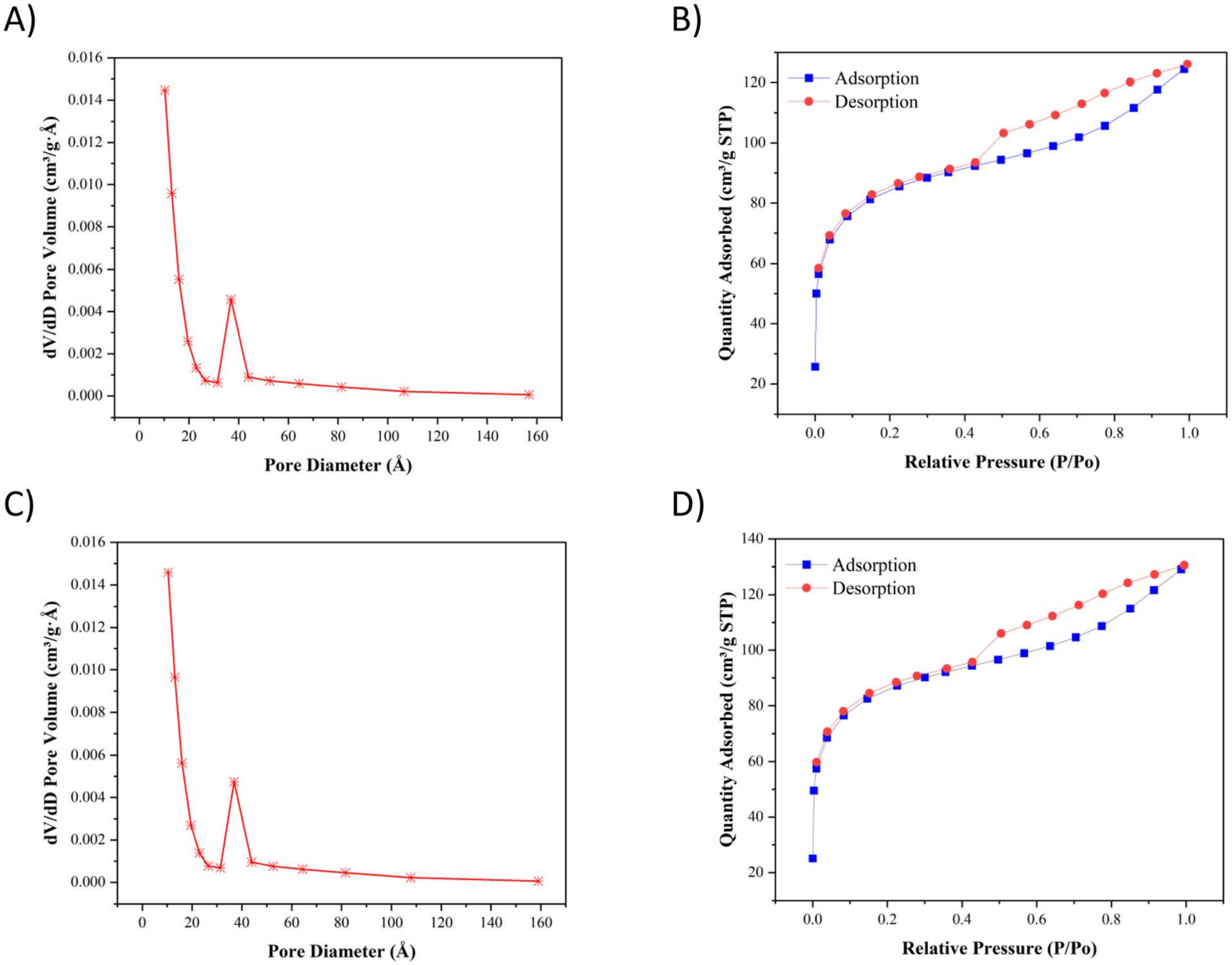

Fig. 6 (A) Pore size distribution of SPCA before MO adsorption; (B) adsorption–desorption nitrogen isotherms of SPCA before MO adsorption; (C) pore size distribution of SPCA after MO adsorption; (D) adsorption–desorption nitrogen isotherms of SPCA after MO adsorption.

MO uptake, the surface area decreases slightly to 254.21 m^2 g^{-1}, indicating partial occupation of accessible adsorption sites by MO molecules rather than structural collapse of the porous network. More pronounced changes are observed in the pore volume parameters. The BJH pore volume derived from N_2 adsorption decreases from 0.119 to 0.099 cm^3 g^{-1}, while the desorption-derived pore volume declines from 0.178 to 0.159 cm^3 g^{-1} after MO adsorption. This reduction provides strong evidence that MO molecules preferentially infiltrate and occupy the internal pore space, particularly mesopores and smaller interconnected pores, leading to a decrease in available void volume. Such behavior is characteristic of adsorption governed by pore-filling mechanisms rather than mere surface coverage.

Consistently, the average pore diameter also decreases after adsorption, from 25.45 to 22.17 Å (adsorption branch) and from 19.33 to 17.12 Å (desorption branch). This shrinkage in effective pore size further supports the conclusion that MO molecules are retained within the pore channels, narrowing the accessible pore width without fundamentally altering the pore geometry. The N_2 adsorption–desorption isotherms of SPCA, both before and after MO adsorption, can be classified as type IV according to IUPAC standards, which is typical of mesoporous materials. The presence of a distinct hysteresis loop in the relative pressure range of $P/P_0 \approx 0.4$–0.9 confirms the occurrence of capillary condensation within mesopores. Notably, the hysteresis loop persists after MO adsorption, although with a slightly reduced adsorbed volume, demonstrating that the mesoporous framework remains structurally intact. The loop shape resembles H3/H4-type hysteresis, suggesting slit-like pores associated with plate-like or layered structural units, which are particularly advantageous for the adsorption of planar aromatic dye molecules such as methyl orange. Overall, the combined BET, BJH, and isotherm analyses reveal that MO adsorption induces measurable but moderate reductions in surface area, pore volume, and pore diameter, all of which are attributable to effective pore filling rather than pore destruction.

As shown in Fig. 7, the surface morphology of SPCA particles prior to adsorption (Fig. 7A–C) reveals a highly irregular and heterogeneous structure characterized by abundant pores, voids, and surface asperities distributed over multiple length scales. At low magnification (×10), the particles exhibit a nearly spherical morphology with a rough outer surface, suggesting successful bead formation and structural integrity. At higher magnifications (×1000 and ×5000), a well-developed porous

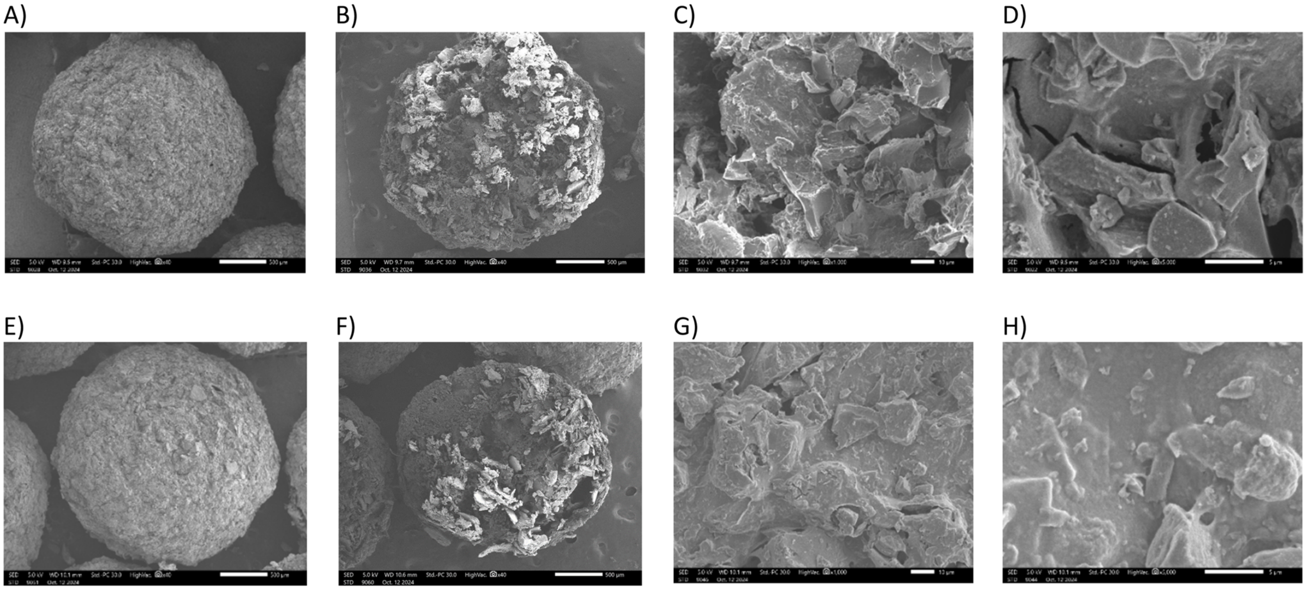

Fig. 7 SEM images of the surface and the cross-sectional morphology of SPCA particles before (A, C, D and B) and after MO adsorption (E, G, H, and F) at magnifications of ×10, 40, 1000 and 5000, respectively.

network composed of interconnected micro- and mesopores becomes evident. This hierarchical porosity is expected to significantly enhance the specific surface area and facilitate rapid mass transfer of dye molecules from the bulk solution to internal adsorption sites.

After MO adsorption (Fig. 7D–F), pronounced morphological changes are observed. The surface appears notably smoother and more compact, with a substantial reduction in visible pores and voids. At higher magnification, the pore openings and interstitial spaces are partially or completely filled, indicating that MO molecules have penetrated and occupied the internal porous network rather than merely adsorbing on the external surface. The coverage of pore walls and surface asperities by adsorbed species suggests strong interactions between MO molecules and the functional groups (–OH, $-COO^-$, and $-NH_2$) distributed throughout the SPCA matrix. Notably, the absence of structural collapse or particle fragmentation after adsorption demonstrates the mechanical robustness of the SPCA beads, which can be attributed to the dual crosslinked polymer network formed *via* Zn^{2+} ionic coordination and glutaraldehyde covalent bonding. These SEM observations are in good agreement with the BET surface area reduction after adsorption and the kinetic results indicating rapid uptake followed by intraparticle diffusion-controlled equilibrium. Overall, the SEM analysis provides direct visual evidence that MO adsorption proceeds through pore filling and surface coverage within a stable, hierarchical porous architecture, confirming the suitability of SPCA as an efficient and structurally durable adsorbent.

Moreover, Fig. 7B and F presents SEM images of the cross-sectional morphology of the SPCA particles before and after methyl orange (MO) adsorption. Prior to adsorption (Fig. 7B), the SPCA particles exhibit a relatively rough and heterogeneous surface with numerous irregular protrusions and fragmented structures distributed across the particle surface. The composite bead displays a compact but hierarchically textured morphology, suggesting the successful integration of the polymeric matrix with the activated carbon component. Such a morphology likely originates from the partial collapse of the polymer network during the drying process, which generates microvoids and surface asperities. These structural irregularities are beneficial for adsorption because they increase the effective surface area and provide abundant accessible active sites for dye molecules. In addition, the presence of loosely aggregated flake-like and granular features on the surface indicates that the composite contains exposed carbonaceous domains embedded within the biopolymer matrix. These domains may contribute to adsorption through multiple interaction mechanisms, including π–π stacking interactions between the aromatic rings of MO molecules and the graphitic structures of activated carbon, as well as electrostatic interactions with protonated functional groups of the polymeric components. After adsorption (Fig. 7F), the overall morphology of the SPCA particles remains largely preserved, indicating that the composite possesses good structural stability during the adsorption process. However, several noticeable morphological changes can be observed.

The surface appears partially covered by aggregated deposits and layered structures, which are likely associated with the accumulation of adsorbed MO molecules within surface cavities and on exposed adsorption sites. In addition, some of the initially visible surface irregularities appear smoother or partially masked after adsorption, suggesting that dye molecules occupy surface defects, pores, and adsorption-active regions. Furthermore, the presence of clustered deposits on the particle surface after adsorption may indicate the formation of localized adsorption domains, where dye molecules accumulate through intermolecular interactions and surface complexation. This observation supports the multilayer adsorption behavior inferred from the Freundlich isotherm model. Importantly, no obvious structural collapse, cracking, or fragmentation of the SPCA. Particles is observed after adsorption, confirming the mechanical robustness and stability of the composite material in aqueous environments. Overall, the SEM observations provide direct morphological evidence supporting the adsorption process. The rough and heterogeneous surface of SPCA offers abundant adsorption sites and facilitates mass transfer of dye molecules from the bulk solution to the internal structure of the composite. The morphological changes observed after adsorption further confirm the successful uptake of MO molecules while demonstrating that the composite retains its structural integrity, which is essential for practical adsorption and regeneration applications.

3.3. Decolorization of MO

3.3.1. Effect of pH. As illustrated in Fig. 8A, solution pH exerts a critical influence on both the adsorption behavior of SPCA and the reliability of adsorption quantification. At strongly acidic conditions (pH 2–3), relatively high apparent adsorption efficiencies and capacities were observed. However, under these conditions, a noticeable shift in the characteristic absorption wavelength ($\lambda_{\max}$) of MO occurred due to pH-induced structural transformation of the dye molecules. Specifically, MO undergoes protonation and tautomeric rearrangement in highly acidic media, leading to spectral shifts that compromise the accuracy of residual concentration determination by UV-vis spectroscopy. Consequently, the adsorption data obtained at pH 2–3 cannot be considered fully reliable for quantitative evaluation. In the alkaline region (pH 6–9), the adsorption efficiency exhibits an increasing trend, which can be attributed to enhanced electrostatic interactions between the adsorbent surface and MO species. Nevertheless, this pH range is accompanied by progressive dissolution of the SPCA beads, arising from the disruption of ionic crosslinks and hydrogen bonding within the polymer network under alkaline conditions. The partial degradation of the adsorbent not only undermines mechanical integrity but also limits its practical applicability, despite the seemingly favorable adsorption performance. At pH 5, the SPCA material maintains good structural stability, and no wavelength shift of MO is detected, ensuring reliable UV-vis

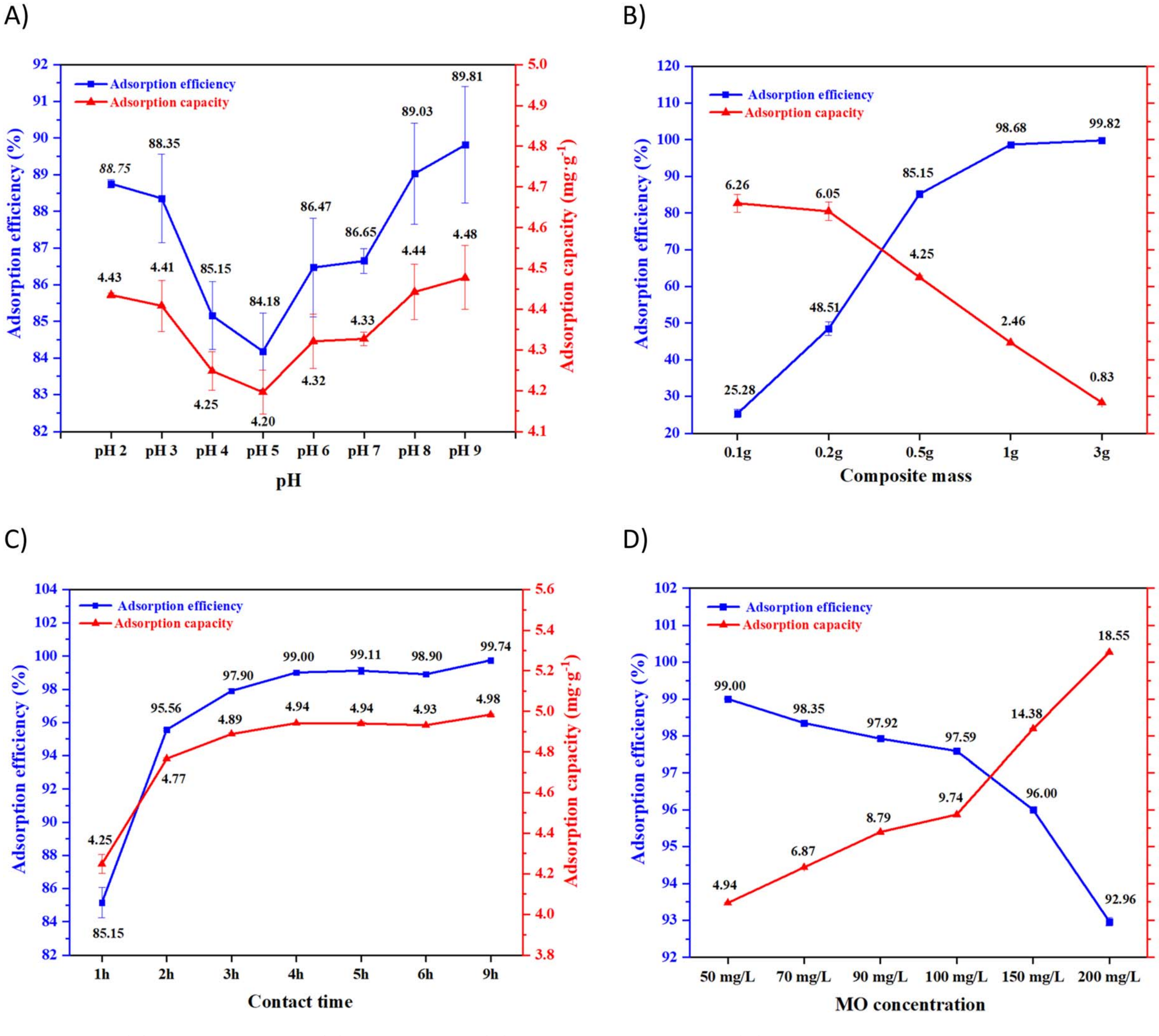

Fig. 8 Effect of pH (A), composite mass (B), contact time (C) and MO concentration (D) for the adsorption efficiency MO.

measurements. However, both adsorption efficiency and adsorption capacity are comparatively low at this pH, indicating suboptimal interaction between MO molecules and the available adsorption sites. Notably, pH 4 emerges as the optimal operational condition, where the adsorption efficiency and adsorption capacity reach approximately 85.15 ± 0.93% and 4.25 ± 0.05 mg g^{-1}, respectively. At this pH, the SPCA beads retain excellent mechanical integrity, no dissolution is observed, and the absorption spectrum of MO remains unchanged, ensuring accurate and reproducible concentration analysis. The favorable adsorption performance at pH 4 can be attributed to strong electrostatic attraction between protonated amino groups ($–NH_3^+$) of chitosan and the anionic sulfonate groups ($–SO_3^-$) of MO, while preserving the structural stability of the composite network. Overall, these results demonstrate that pH 4 represents the most appropriate compromise between adsorption efficiency, material stability, and analytical reliability, and was therefore selected as the optimal pH for subsequent adsorption experiments.

3.3.2. Effect of composite mass. As shown in Fig. 8B, the dosage of SPCA beads exerts a pronounced and non-linear influence on both adsorption efficiency and adsorption capacity, reflecting the interplay between the availability of active sites and their effective utilization. At low adsorbent dosages (0.1–0.2 g), the adsorption efficiency remains limited (25.28% and 48.51%, respectively), which can be attributed to the insufficient number of accessible adsorption sites relative to the fixed amount of MO in solution. Under these conditions, the adsorption process is site-limited, and a large fraction of dye molecules remains unadsorbed. Increasing the adsorbent mass to 0.5 g results in a sharp improvement in adsorption efficiency to 85.15 ± 0.93%, accompanied by an adsorption capacity of 4.25 ± 0.05 mg g^{-1}. This dosage represents an optimal balance between surface site availability and effective site utilization. At this level, the number of adsorption sites is sufficient to capture a substantial fraction of MO molecules, while mass-transfer resistance and particle aggregation remain minimal, allowing efficient intraparticle diffusion and surface interaction. Further increasing the adsorbent mass to 1 and 3 g leads to a continued rise in adsorption efficiency, reaching 98.68% and 99.82%, respectively. However, this improvement is accompanied by a pronounced decline in adsorption capacity to 2.46 and 0.83 mg g^{-1}, indicating a substantial underutilization of the available adsorption surface. This behavior is commonly attributed to the overlapping and shielding of adsorption sites, as well as the establishment of a concentration gradient where the amount of dye becomes insufficient to occupy all available active sites. Consequently, a significant portion of the adsorbent remains unused, resulting in inefficient material utilization and increased operational cost. Therefore, a dosage of 0.5 g was selected as the optimal adsorbent mass for subsequent experiments, as it provides a favorable compromise between high adsorption efficiency, reasonably high adsorption capacity, and economical use of the adsorbent. This selection is particularly relevant for practical wastewater treatment applications, where maximizing dye removal while minimizing material consumption is essential.

3.3.3. Effect of contact time. As illustrated in Fig. 8C, contact time exerts a decisive influence on the adsorption behavior of MO onto SPCA beads. The contact-time experiments were conducted at an initial MO concentration of 50 mg L^{-1}, an adsorbent dosage of 0.5 g, and a solution volume of 50 mL under the previously optimized pH conditions. The observed adsorption capacity values (approximately 4–5 mg g^{-1} at equilibrium) are therefore consistent with the relatively low initial dye concentration employed in this series of experiments. During the initial stage (1–2 h), adsorption proceeded rapidly, with removal efficiency increasing from 85.15% at 1 h to 95.56% at 2 h, while the adsorption capacity increased from 4.25 to 4.77 mg g^{-1}. This rapid uptake is attributed to the abundance of available active sites on the external surface of the beads and the high concentration gradient between the bulk solution and the adsorbent surface, which promotes fast surface adsorption. As the contact time increased to 3–4 h, the adsorption rate gradually decreased and the system approached equilibrium. At 4 h, the removal efficiency and adsorption capacity reached 99.00% and 4.94 mg g^{-1}, respectively, indicating that most accessible adsorption sites had been occupied under these concentration conditions. In this stage, intraparticle diffusion becomes increasingly significant, as MO molecules diffuse into the internal porous network of the composite beads, resulting in slower adsorption kinetics. Further extension of the contact time beyond 4 h (up to 5, 6, and 9 h) led to only marginal changes in removal efficiency (99.11–99.74%) and adsorption capacity (4.94–4.98 mg g^{-1}). This negligible improvement confirms that adsorption equilibrium had been effectively established at 4 h. Therefore, a contact time of 4 h was selected as the optimal adsorption duration for subsequent experiments.

3.3.4. Effect of MO concentration. As depicted in Fig. 8D, the initial MO concentration significantly influences both removal efficiency and adsorption capacity. The concentration-dependent experiments were conducted at pH 4, an adsorbent dosage of 0.5 g, a solution volume of 50 mL, and a contact time of 4 h. At low initial concentrations (50–100 mg L^{-1}), removal efficiency remained very high, decreasing slightly from 99.00% (50 mg L^{-1}) to 97.59% (100 mg L^{-1}), while adsorption capacity increased proportionally from 4.94 to 9.74 mg g^{-1}. Under these dilute conditions, the number of available adsorption sites greatly exceeded the number of MO molecules, resulting in near-complete dye removal. As the initial concentration increased to 150 mg L^{-1}, the adsorption capacity rose markedly to 14.38 ± 0.02 mg g^{-1}, accompanied by a moderate decrease in removal efficiency to 96.00 ± 0.02%. This behavior reflects an increased mass-transfer driving force and more effective utilization of internal adsorption sites. At the highest tested concentration (200 mg L^{-1}), adsorption capacity further increased to 18.55 mg g^{-1}, whereas removal efficiency decreased to 92.96%, indicating progressive saturation of available adsorption sites. Although the highest adsorption capacity was obtained at 200 mg L^{-1}, the condition of 150 mg L^{-1} was selected for subsequent investigations as a practical compromise between high dye removal efficiency and substantial adsorption capacity. Under these conditions (pH 4, 0.5 g adsorbent, 50 mL solution, 4 h contact time, and 150 mg L^{-1} MO), SPCA exhibited 96.00% removal efficiency with an adsorption capacity of 14.38 mg g^{-1}.

Overall, the adsorption parameter optimization was conducted systematically by varying pH, adsorbent dosage, contact time, and initial MO concentration. It should be noted that the pH, dosage, and contact-time experiments were performed at an initial MO concentration of 50 mg L^{-1}, whereas the concentration-dependent study was carried out over a wider range of 50–200 mg L^{-1}. Although slightly higher removal efficiencies were observed at alkaline pH values (pH 8–9), noticeable structural instability and partial dissolution of the composite beads were detected under these conditions. Therefore, pH 4 was selected as the optimal operational pH, as it ensured high adsorption performance while maintaining excellent structural integrity and analytical reliability. Similarly, while the highest adsorption capacity was achieved at 200 mg L^{-1}, the condition of 150 mg L^{-1} was selected for subsequent kinetic, isotherm, and regeneration studies.

This concentration provides a balanced compromise between high adsorption capacity (14.38 mg g^{-1}) and high removal efficiency (96.00%), avoiding excessive site saturation and ensuring stable adsorption behavior. Under the selected optimal conditions (pH 4, 0.5 g adsorbent, 50 mL solution, 4 h contact time, and 150 mg L^{-1} MO), SPCA demonstrated robust adsorption performance without compromising structural stability.

3.4. Adsorption isotherm model

Based on the concentration-dependent adsorption results of MO (Section 3.3.4), the equilibrium adsorption behavior of SPCA was quantitatively evaluated using Langmuir, Freundlich, and Temkin isotherm models (Fig. 9 and Table S2) to elucidate the dominant adsorption mechanism. The Langmuir isotherm, expressed by the linear equation $C_e/q_e = 0.0466\ C_e + 0.1155$, exhibits a high correlation coefficient ($R^2 = 0.9911$), indicating that monolayer adsorption on energetically equivalent sites contributes significantly to MO uptake. This suggests that a portion of the SPCA surface behaves as uniformly accessible adsorption sites, particularly at low to moderate concentrations. However, the Langmuir model inherently assumes a homogeneous surface and neglects lateral interactions between adsorbed molecules, which is inconsistent with the complex, hierarchical pore structure and chemically heterogeneous surface of SPCA. Consequently, while the Langmuir model provides a reasonable approximation, it does not fully capture the intrinsic adsorption behavior of this material. In contrast, the Freundlich isotherm demonstrates the highest fitting accuracy, with the linear form $\ln q_e = 0.4046 \ln C_e + 1.8967$ and an R^2 value of 0.9945. The Freundlich constant n (>1) indicates favorable adsorption and reflects a non-uniform distribution of adsorption energies across the SPCA surface. This behavior is consistent with the presence of heterogeneous functional groups, slit-like mesopores, and variable pore accessibility, as confirmed by BET and SEM analyses. The superior fit of the Freundlich model therefore indicates that MO adsorption on SPCA is governed predominantly by multilayer adsorption on energetically heterogeneous sites rather than ideal monolayer coverage. The Temkin isotherm, with an R^2 value of 0.9779, also provides insight into the adsorption process by accounting for adsorbate–adsorbent interactions and the progressive decrease in adsorption heat with surface coverage.

Although this model captures the general energetic trend of MO adsorption, its relatively lower correlation coefficient suggests limited applicability in describing the full complexity of SPCA, particularly its structural heterogeneity and pore-filling effects. Overall, comparative analysis of the three isotherm models clearly identifies the Freundlich model as the most appropriate descriptor of MO adsorption on SPCA. This conclusion is supported by its highest correlation coefficient and physically meaningful parameters, which collectively indicate heterogeneous surface adsorption with variable binding energies. The isotherm behavior of SPCA is in good agreement with previously reported results for porous carbon-based and biomass-derived adsorbents used for anionic dye removal.[62,63] While the Langmuir and Temkin models contribute complementary insights, the Freundlich model most accurately reflects the dominant adsorption mechanism of SPCA, confirming its suitability for efficient and stable adsorption of MO from aqueous solutions.

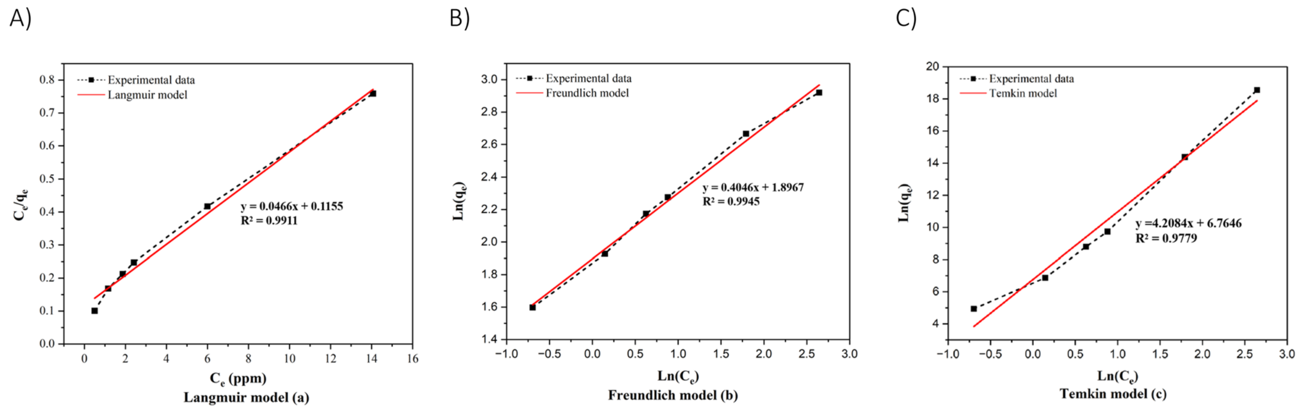

Fig. 9 Adsorption isotherm of Langmuir model (A), Freundlich model (B) and Temkin model (C).

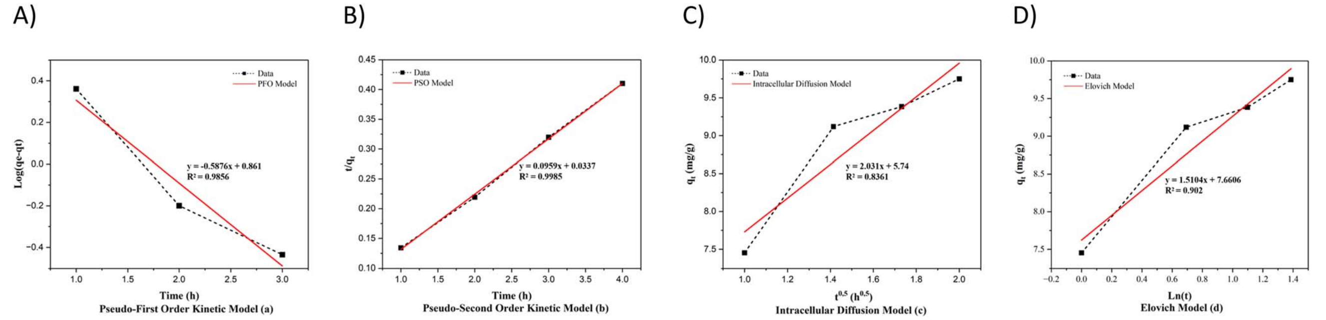

Fig. 10 Pseudo-first-order kinetic model (A), pseudo-second-order kinetic model (B), intracellular diffusion model (C) and Elovich kinetic model (D).

3.5. Adsorption kinetics model

The adsorption kinetics of MO onto SPCA were systematically analyzed using pseudo-first-order (PFO), pseudo-second-order (PSO), Elovich, and intraparticle diffusion models, as presented in Fig. 10 and Table S3. Comparative evaluation of correlation coefficients (R^2) and calculated equilibrium adsorption capacities ($q_{e,cal}$) provides insight into the dominant rate-controlling mechanisms. The PFO model exhibits a relatively high correlation coefficient ($R^2 = 0.9856$), indicating that it can partially describe the early stage of the adsorption process. However, the calculated equilibrium adsorption capacity ($q_{e,cal} = 7.26$ mg g^{-1}) is significantly lower than the experimental value ($q_{e,exp} = 9.51$ mg g^{-1}). This discrepancy suggests that adsorption is not governed solely by physical diffusion or external surface interactions. The deviation is likely attributable to the heterogeneous surface chemistry and pore structure of SPCA, which leads to time-dependent variations in adsorption rates and limits the applicability of the PFO model, particularly near equilibrium. In contrast, the PSO model provides an excellent fit to the experimental data, with the highest correlation coefficient ($R^2 = 0.9985$) and a calculated adsorption capacity ($q_{e,cal} = 10.42$ mg g^{-1}) in close agreement with the experimental value. The superior performance of the PSO model indicates that the adsorption process is predominantly controlled by chemisorption, involving valence forces through electron sharing or exchange between MO molecules and active functional groups on the SPCA surface. This behavior is consistent with the presence of abundant oxygen- and nitrogen-containing functional groups derived from the biopolymer matrix and activated carbon component, which can form strong interactions with anionic dye molecules. The Elovich model yields a moderate correlation coefficient ($R^2 = 0.9020$), suggesting that while surface heterogeneity and exponential decreases in adsorption rate may occur, these effects are not the dominant factors governing the overall adsorption kinetics.

Although the Elovich model is often applicable to highly heterogeneous systems, its lower fitting accuracy compared to the PSO model indicates limited relevance for quantitatively describing the MO adsorption process on SPCA. The intraparticle diffusion model exhibits the lowest correlation coefficient ($R^2 = 0.8361$), indicating that intraparticle diffusion is not the sole rate-limiting step. This implies that adsorption proceeds through multiple stages, including external surface adsorption followed by gradual diffusion into internal pores. However, since the model does not pass through the origin, intraparticle diffusion acts as a secondary or supportive mechanism rather than the primary kinetic control. Overall, the kinetic study unequivocally indicates that the pseudo-second-order model most precisely characterizes the adsorption behavior of MO onto SPCA. This verifies that chemisorption is the prevailing mechanism, likely due to robust electrostatic attraction between protonated amino groups and sulfonate groups of MO, in conjunction with hydrogen bonding and π–π interactions, whereas physical diffusion and intraparticle transport play a contributory role but do not govern the overall adsorption rate.

3.6. Adsorption mechanism

These findings are in good agreement with previously reported adsorption kinetics for porous, biomass-derived composite adsorbents used in dye removal systems,[32,63] further validating the effectiveness and mechanistic consistency of SPCA as an efficient adsorbent. Based on the convergence of kinetic data, isotherm modeling, spectroscopic characterization, and

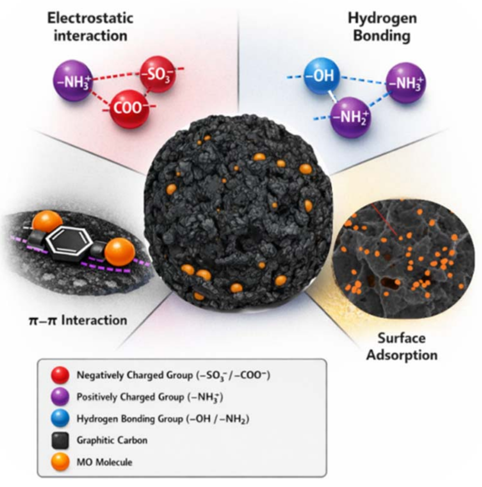

Fig. 11 The schematic illustration of the possible adsorption mechanism of SPCA for MO.

textural analysis, the adsorption of MO onto the SPCA composite is governed by four synergistic physicochemical mechanisms that operate simultaneously and whose relative contributions evolve across the adsorption timeline. The proposed mechanism is illustrated schematically in Fig. 11 with four ways as follows:

(i) Electrostatic attraction. The dominant interaction driving MO uptake onto SPCA at pH 4 is direct electrostatic attraction between the protonated amino groups ($-NH_3^+$) of chitosan and the anionic sulfonate group ($-SO_3^-$) of MO. At pH values below the pK_a of chitosan (∼6.3–6.5), the primary amine functions are quantitatively protonated, generating a high surface density of positively charged sites.[34] These $-NH_3^+$ species form a stable ionic pair with the $-SO_3^-$ moiety of MO, constituting a chemisorption-type interaction that is fully consistent with the pseudo-second-order kinetic behavior observed experimentally ($R^2 = 0.9985$) – a hallmark of charge-transfer-mediated surface binding.[32] The pH-dependence of the adsorption capacity – with a clear maximum at pH 4 and progressive decline toward alkalinity – corroborates the central role of protonated amino groups: as pH increases beyond the pK_a of chitosan, $-NH_3^+$ undergoes deprotonation to $-NH_2$, reducing the density of cationic sites and consequently diminishing the electrostatic driving force for MO uptake. Furthermore, the systematic enhancement in adsorption capacity as chitosan content increases from 1% to 4% provides additional direct evidence that $-NH_3^+$ group density is the primary determinant of MO removal efficiency.[34] Importantly, as demonstrated in analogous composite adsorbent systems, electrostatic attraction constitutes one component of a broader physicochemical synergy in which multiple simultaneous mechanisms collectively determine adsorption performance.[64]

It is essential to clarify that the carboxylate groups ($-COO^-$) of alginate and pectin, while structurally abundant in SPCA, do not contribute directly to electrostatic MO uptake: the anionic character of both $-COO^-$ and $-SO_3^-$ precludes attractive electrostatic interaction between these groups and the MO anion. Instead, $-COO^-$ groups fulfill a dual structural and adsorption-assisting function. Structurally, they coordinate with Zn^{2+} ions to form the classical "egg-box" crosslinked network, as evidenced by the characteristic shift of the asymmetric $-COO^-$ stretching band from ∼1631 cm^{-1} in the pristine polymers to ∼1627 cm^{-1} in SPCA.[48] In terms of adsorption, they contribute indirectly through hydrogen bonding (mechanism ii, below) and by maintaining the open, swellable pore architecture that supports intraparticle transport.[12]

(ii) Hydrogen bonding. A secondary yet significant contribution to MO retention arises from multiple hydrogen bonding interactions between the oxygen-containing functional groups of the biopolymer matrix and the structural features of MO. The hydroxyl groups (–OH) present in the pyranose rings of alginate, pectin, and chitosan function as both hydrogen bond donors and acceptors toward the azo linkage (–N=N–), the dimethylamino group ($-N(CH_3)_2$), and the sulfonate group ($-SO_3^-$) of MO.[12,13] Partially protonated carboxylate groups (–COOH) at pH 4 further contribute as strong hydrogen bond donors toward the nitrogen and oxygen atoms of the dye molecule.[14] Spectroscopic evidence for hydrogen bond formation is provided by the FTIR analysis of SPCA after MO adsorption: the –OH stretching envelope (3300–3450 cm^{-1}) exhibits measurable broadening and a slight bathochromic shift relative to the pre-adsorption spectrum, consistent with the formation of new intermolecular hydrogen bonds between adsorbent surface groups and adsorbed MO species.[41,42] Hydrogen bonding is also mechanistically compatible with the multilayer adsorption behavior described by the Freundlich isotherm ($R^2 = 0.9945$): once the first monolayer of MO is anchored to SPCA surface sites through electrostatic attraction, subsequent MO molecules may interact with the already-adsorbed layer through intermolecular hydrogen bonds and dipole–dipole interactions, generating the heterogeneous multilayer stacking captured by the Freundlich model.[32] The important role of surface hydroxyl groups in facilitating hydrogen bond-mediated pollutant retention has been highlighted in mechanistic studies of bio-composite adsorbent systems.[64]

(iii) π–π Stacking interactions. The incorporation of activated carbon (AC) introduces a third adsorption pathway through non-covalent π–π electron donor–acceptor interactions between the graphitic micro-domains of AC and the extended aromatic conjugation system of MO. The molecular structure of MO features two phenyl rings connected through an azo bridge (–N=N–) with a dimethylamino electron-donating substituent and a sulfonate electron-withdrawing group, constituting a highly polarized, delocalized π-electron system. The turbostratic carbon structure of AC, confirmed by the broad XRD reflection at $2\theta \approx 26°$ corresponding to the graphitic plane,[57] provides a complementary π-electron-rich surface that engages in face-to-face or edge-to-face π–π stacking with the aromatic rings of MO.[54] The presence of graphitic C=C stretching and aromatic C–O vibrations in the FTIR spectrum of SPCA (1500–1600 cm^{-1}) confirms that the carbonaceous domains are surface-exposed and accessible for this interaction.[53] The quantitative contribution of this mechanism is demonstrated by the systematic increase in adsorption capacity from 4.66 to 4.91 mg g^{-1} as AC loading increases from 1% to 4%, an enhancement that exceeds what would be expected from surface area expansion alone and thus reflects a genuine chemical affinity contribution.[29] π–π stacking between carbonaceous domains and the aromatic rings of azo dyes has been extensively documented as a key secondary adsorption mechanism in AC-containing bio-composite systems, augmenting the primary electrostatic driving force.[54,65] This synergistic interplay between surface electrostatics and π–π stacking is mechanistically analogous to the co-occurrence of chemisorption and physical adsorption (Freundlich $n > 1$) reported in multi-mechanism composite adsorbent systems,[64] underscoring the generality of this physicochemical synergy across different pollutant–adsorbent pairs.

(iv) Sureface adsorption. Textural analysis provides direct quantitative evidence for a pore-filling mechanism as the fourth adsorption pathway. BET analysis reveals that MO adsorption induces a statistically significant decrease in BJH pore volume from 0.119 to 0.099 cm^3 g^{-1} (adsorption branch) and from 0.178

to 0.159 $cm^3 g^{-1}$ (desorption branch), and a contraction of the average pore diameter from 25.45 to 22.17 Å (adsorption branch), while the specific surface area remains essentially unchanged (255.88 *vs.* 254.21 $m^2 g^{-1}$), collectively indicating that MO molecules preferentially penetrate and occupy the internal mesopore channels rather than adsorbing exclusively on the external particle surface. The type IV N_2 adsorption–desorption isotherms with H3/H4-type hysteresis loops, which persist after MO adsorption with a reduced adsorbed volume, confirm that the mesoporous framework remains structurally intact while partially filled with retained dye.[10,11] The multi-stage intraparticle diffusion kinetics—evidenced by the non-zero intercept ($C > 0$) of the Weber–Morris plot and the three distinct linear regions[33] — confirms that adsorption proceeds through sequential stages: rapid film boundary diffusion and external surface adsorption (Stage 1), followed by slower intraparticle diffusion into the mesopore network as the rate-limiting step (Stage 2), and finally attainment of equilibrium at deeply embedded adsorption sites (Stage 3).[32] SEM morphological analysis provides complementary direct visual evidence: the surface of SPCA after MO adsorption exhibits reduced roughness, partial occlusion of visible pore openings, and the formation of localized dye deposits within surface cavities (Fig. 7D–H), fully consistent with a pore-filling mechanism. The critical role of pore structure and interlayer/pore spacing in accommodating adsorbate species through multilayer mechanisms has been identified as a governing factor in optimized composite adsorbent systems,[64] reinforcing the conclusion that textural optimization is as important as surface chemistry in determining the ultimate adsorption capacity.

The four mechanisms described above do not operate independently but evolve in their relative contributions across the adsorption timeline. During the initial rapid phase (0–2 h), adsorption is dominated by electrostatic attraction and hydrogen bonding at the readily accessible external surface and large mesopore openings, driven by a high MO concentration gradient (removal efficiency: 85.15% → 95.56%). As the contact time extends (2–4 h), intraparticle diffusion becomes rate-limiting as MO molecules migrate progressively deeper into the porous composite structure,[32] and π–π stacking interactions with AC domains become increasingly relevant at internal adsorption sites.[54] At equilibrium (4 h), all four mechanisms collectively determine the total adsorption capacity, with the heterogeneous multilayer distribution of retained MO described by the Freundlich model ($R^2 = 0.9945$).[32] These findings are in good agreement with previously reported adsorption kinetics for porous, biomass-derived composite adsorbents used in dye removal systems[32,63] and with multi-mechanism characterizations of optimized bio-composite adsorbents,[64] further validating the effectiveness and mechanistic consistency of SPCA as an efficient and structurally durable adsorbent for the removal of anionic azo dyes from aqueous media. The mechanistic schematic incorporating all four pathways and the temporal sequence of their activation is presented in Fig. 11.

3.7. Desorption and recyclability studies

3.7.1. Effect of desorption solvent. The influence of different desorption solvents on the structural stability and regeneration performance of SPCA was systematically evaluated, as illustrated in Fig. 12. Under alkaline conditions (0.1 N NaOH and 0.05 M $NaHCO_3$), the SPCA beads dissolved completely (Fig. 12A and B), indicating severe structural instability. This behavior is attributed to deprotonation of carboxyl and hydroxyl groups within the biopolymeric network, which induces electrostatic repulsion and disrupts Zn^{2+}-mediated ionic crosslinking, ultimately leading to breakdown of the composite structure. Similar alkaline-induced degradation was observed during swelling tests in PBS and has been reported in previous studies.[30] In strongly acidic medium (0.1 N HCl), the

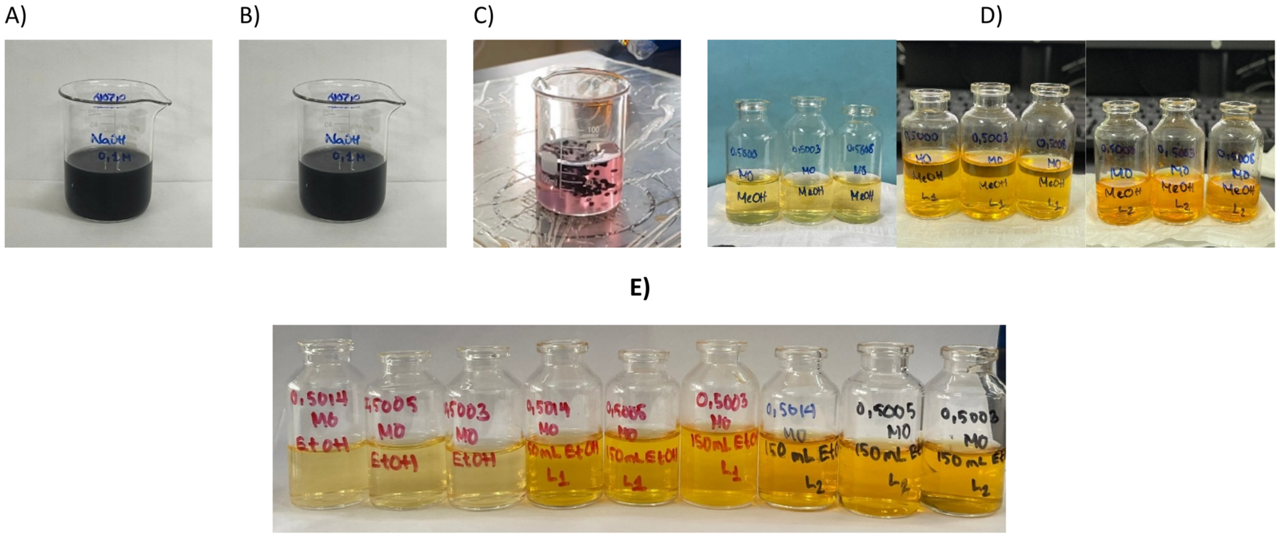

Fig. 12 The effect of different solvents on the MO desorption process of SPCA (A) NaOH 0.1 N; (B) NaHCO3 0.05 M, (C) HCl 0.1 N, (D) MeOH 96% và (E) EtOH 96%.

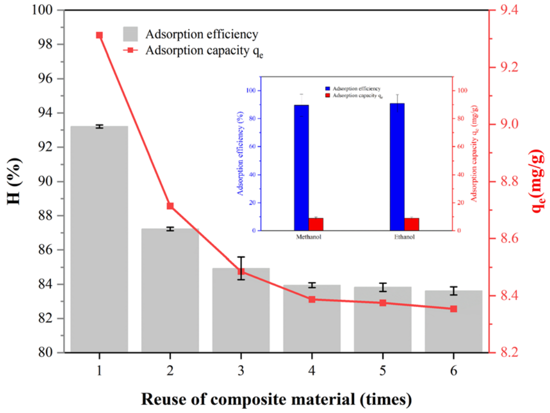

Fig. 13 Reuse of composite materials with 50 mL EtOH.

SPCA beads initially maintained their structural integrity (Fig. 12C); however, a noticeable color shift of methyl orange was observed after regeneration. This phenomenon arises from the pH-dependent structural transformation of MO and possible partial degradation of natural polymer chains under highly acidic conditions. Such effects compromise the reliability of adsorption measurements and limit the suitability of strong acids as regenerating agents. In contrast, organic solvents such as methanol and ethanol (Fig. 12D and E) effectively preserved the structural integrity of SPCA while enabling efficient desorption of MO.

The quantitative results are summarized in figure insert Fig. 13. For methanol, the adsorption efficiency decreased from 96.51% in the first cycle to 80.99% in the third cycle, with an average efficiency of 89.54%. The corresponding adsorption capacity declined from 9.64 to 8.09 mg g^{-1} (average 8.95 mg g^{-1}). The slightly superior performance of ethanol compared to methanol suggests that ethanol better preserves the adsorption-active functional groups and crosslinked network structure during regeneration. Overall, these results demonstrate that ethanol is an effective, mild, and environmentally benign regenerating solvent for SPCA, enabling high desorption efficiency while maintaining structural stability and adsorption performance. This finding highlights the suitability of SPCA for repeated use in wastewater treatment applications.

3.7.2. Recyclability. The recyclability of SPCA using ethanol as the regenerating solvent is illustrated in Fig. 13. As the number of reuse cycles increased, a gradual decline in adsorption performance was observed. Specifically, the adsorption efficiency decreased from 97.96% in the first cycle to 93.21% after one regeneration and further declined to 83.62% after six consecutive cycles. Although this reduction is non-negligible, the rate of performance loss significantly slowed after the second cycle, suggesting that the majority of easily accessible adsorption sites remain active over prolonged reuse. The observed decline in adsorption efficiency and capacity can be primarily attributed to partial mass loss of the composite during regeneration. Ethanol, while chemically mild, can still induce gradual weakening of crosslinked networks by disrupting hydrogen bonding and coordination interactions, particularly those involving metal ions and biopolymer

Table 1 Comparative analysis of polysaccharide-derived adsorbents for dye removal

Adsorbent	Composition/description	q_{max} (mg g^{-1})	Optimal pH	Kinetic model	Isotherm model	Reuse cycles (%)	Reference
Chitosan–alginate composite (Cs-F-An)-G-Al	Aniline-modified chitosan crosslinked with alginate *via* glutaraldehyde	198.09	6.0	PSO	Langmuir	—	66
Chitosan–biochar microspheres (CS-PABC)	Chitosan encapsulating palmer amaranth biochar; batch adsorption	495.0–554.3 (25–45 °C)	3.0	PSO	Langmuir	—	67
Chitosan-modified biochar (CSBC)	Shrimp-shell chitosan coating on rice husk biochar hydrogel beads	17.58	3.0	PSO + intraparticle diff	Langmuir	—	68
Poultry manure-derived biochar (PM-BC)	Slow pyrolysis at 550 °C; SBET 16.09 m^2 g^{-1}	20.80	4.0	PSO	Langmuir	—	69
Nitrogen-rich biomass-derived carbon (N-BC)	Enteromorpha-derived biochar; multi-stage adsorption; DFT-supported	269.58	3–4	PSO	Langmuir/Freundlich	—	70
PAAM/chitosan hydrogel	Semi-IPN of polyacrylamide and chitosan; photo-polymerization	202.02	3.0	PSO	Langmuir	Reusable	71
CS-EGDE biofilm	Crosslinked chitosan–ethylene glycol diglycidyl ether biofilm on glass	131.2	—	PSO	Langmuir	Reusable	72
SPCA composite	*Opuntia dillenii* pectin + alginate + chitosan + activated carbon; dual Zn^{2+} ionic + glutaraldehyde covalent crosslinking; hierarchical mesoporous; air-dried beads	18.55/14.38	4.0	PSO ($R^2 = 0.9985$)	Freundlich ($R^2 = 0.9945$)	6 cycles (83.62%)	This work

functional groups. This phenomenon has also been reported by Guibal and co-workers,[28] who attributed similar performance degradation to solvent-induced structural fatigue during repeated adsorption–desorption cycles. Despite this limitation, the ability of SPCA to retain more than 80% of its initial adsorption efficiency after six cycles highlights its remarkable structural robustness and practical viability. Such performance compares favorably with many reported bio-based adsorbents, underscoring the potential of SPCA as a sustainable and reusable material for dye-contaminated wastewater treatment. Future optimization strategies, such as enhancing crosslinking density or introducing more stable coordination sites, may further improve regeneration stability and extend the operational lifespan of the composite (Table 1).

Compared with other materials in the table, SPCA in this study exhibits a relatively lower adsorption capacity ($q_{\max}$ ~18.55 mg g^{-1}) than several advanced systems such as chitosan–biochar (~495–554 mg g^{-1}) or PAAM/chitosan hydrogels (~202 mg g^{-1}), indicating that it is not optimized for maximum adsorption performance. However, the key strength of SPCA lies in its renewable bio-based feedstock (pectin from *Opuntia dillenii*) and green, mild synthesis conditions, whereas many other materials rely on intensive chemical modification or more complex fabrication processes. In addition, SPCA follows a Freundlich isotherm, suggesting heterogeneous multilayer adsorption consistent with its composite structure, in contrast to the Langmuir behavior commonly reported for other systems.

In terms of applicability, SPCA achieves high removal efficiency (~96%) at practical concentrations and demonstrates reusability over six cycles (83.62%), which is comparable to or clearer than several materials that only report being "reusable" without detailed cycling data. Its granular structure also facilitates separation and handling, offering an advantage over powder or hydrogel systems. Nevertheless, limitations remain, including moderate adsorption capacity, reduced stability under alkaline conditions, and gradual performance decline upon reuse, whereas some inorganic or nanostructured materials exhibit superior durability. Overall, this work stands out for its sustainability, cost-effectiveness, and practical potential, although further improvements in adsorption capacity and long-term stability are needed to compete with high-performance engineered adsorbents.

4. Conclusions

In this study, a novel bio-based composite adsorbent (SPCA) was successfully designed and fabricated using *Opuntia dillenii*-derived pectin in combination with sodium alginate, chitosan, activated carbon, and environmentally benign additives. The composite was synthesized under mild conditions and formed stable granular particles with an amorphous structure. Comprehensive physicochemical characterizations confirmed the successful integration of the constituent polymers into an interconnected porous network, resulting in enhanced mechanical integrity and thermal stability compared with the individual raw materials. The optimized SPCA formulation exhibited excellent adsorption performance toward MO, achieving a maximum adsorption capacity of 18.55 mg g^{-1} at an initial concentration of 200 mg L^{-1}, while an adsorption capacity of 14.38 mg g^{-1} with 96.0% removal efficiency was obtained under the selected optimal operating concentration of 150 mg L^{-1}. Adsorption kinetics were best described by the pseudo-second-order model ($R^2 = 0.9985$), indicating that chemisorption plays a dominant role in the adsorption process. Equilibrium data followed the Freundlich isotherm model ($R^2 = 0.9945$), revealing multilayer adsorption on a heterogeneous surface, which is consistent with the complex morphology and functional group diversity of the composite. Notably, the SPCA adsorbent demonstrated good regeneration and reuse capability. When ethanol was employed as a green desorbing agent, the composite retained 83.62% of its initial adsorption efficiency and an adsorption capacity of 8.35 mg g^{-1} after six adsorption–desorption cycles. However, the inherent variability of *O. dillenii* biomass due to seasonal and geographic factors remains a challenge for large-scale standardization. Operationally, the SPCA composite exhibits alkaline instability due to the disruption of Zn^{2+}-mediated crosslinks, limiting its application to acidic conditions (pH < 5) and necessitating pre-acidification for neutral or alkaline effluents. Furthermore, this study was conducted exclusively with single-component MO solutions under controlled conditions, meaning the performance of SPCA in real industrial wastewaters containing multiple dyes and competing ions remains to be evaluated. Despite gradual mass loss and a moderate decline in adsorption performance during repeated reuse, the SPCA adsorbent retained substantial adsorption effectiveness, highlighting its structural robustness and practical applicability. Moreover, its adsorption capacity is moderate compared with some highly engineered adsorbents, SPCA offers several important advantages, including green synthesis, renewable biomass utilization, structural stability, and reusability—features that are essential for practical wastewater treatment.

Author contributions

Thi-Kim-Chi Huynh: conceptualization, data curation, funding acquisition, investigation, methodology, project administration, resources, supervision, validation, writing – original draft, writing – review & editing; Thi-Hong-An Nguyen, and Cong-Hau Huynh: data curation, formal analysis, software, validation, visualization, writing – original draft; Xuan-Ngoc Nguyen, Thi-Cam-Thu Nguyen, Hoang-Phuc Nguyen: data curation, formal analysis, software, visualization, writing – original draft; Anh-Khoa Ton, Thanh-Danh Nguyen, Thi Be Ta Truong, Thi-Thanh-Tu Nguyen, Chien Phuong Tran, Thi-Kim-Dung Hoang: formal analysis, methodology, validation, writing – original draft.

Conflicts of interest

There are no conflicts to declare.

Data availability

All required data supporting the findings are available in the manuscript. The data supporting this article have been included as part of the supplementary information (SI). Supplementary information is available. See DOI: https://doi.org/10.1039/d6ra02331b.

Acknowledgements

This research is funded by Vietnam Academy of Science and Technology under grant number VAST07.02/24-25.

References

1 K. Akansha, A. N. Yadav, M. Kumar, D. Chakraborty and S. J. F. M. Ghosh Sachan, *Folia Microbiol.*, 2022, **67**, 91–102.
2 A. Das and M. Susmita, *Int. J. Curr. Microbiol. Appl. Sci.*, 2016, **5**, 675–686.
3 T. Akter, A. T. Protity, M. Shaha, M. Al Mamun and A. Hashem, in *Nanohybrid Materials for Treatment of Textiles Dyes*, Springer, 2023, pp. 401–431.
4 T. Islam, M. R. Repon, T. Islam, Z. Sarwar and M. M. Rahman, *Environ. Sci. Pollut. Res.*, 2023, **30**, 9207–9242.
5 M. Ismail, K. Akhtar, M. Khan, T. Kamal, M. A. Khan, A. M Asiri, J. Seo and S. B. Khan, *Curr. Pharm. Des.*, 2019, **25**, 3645–3663.
6 F. Tian, Y. Wang, G. Guo, K. Ding, F. Yang, H. Wang, Y. Cao and C. J. B. T. Liu, *Bioresour. Technol.*, 2021, **326**, 124749.
7 M. A. El-Rahman, A. Z. Omar, A. R. Kandeel, E. A. Hamed, M. A. El-Atawy and R. M. Keshk, *Sci. Rep.*, 2025, **15**, 13410.
8 A. Pandey, V. M. Pathak and M. Rajput, *Heliyon*, 2024, **10**, e32339.
9 Y.-N. Liu, F. Zhang, J. Li, D.-B. Li, D.-F. Liu, W.-W. Li and H.-Q. Yu, *Environ. Sci. Technol.*, 2017, **51**, 8616–8623.
10 J. Ma, F. Yu, L. Zhou, L. Jin, M. Yang, J. Luan, Y. Tang, H. Fan, Z. Yuan and J. Chen, *ACS Appl. Mater. Interfaces*, 2012, **4**, 5749–5760.
11 I. Daou, Y. Dehmani, H. Moussout, D. S. Franco, J. Georgin, M. E. Bakkali, M. Tahaikt, A. Shaim, O. Zegaoui and S. Abouarnadasse, *Environ. Monit. Assess.*, 2024, **196**, 1057.
12 J. Lu, Y. Zhou and Y. Zhou, *Crit. Rev. Environ. Sci. Technol.*, 2023, **53**, 1709–1730.
13 M. Khatri, R. A. Al-Juboori, M. Mehdi, N. K. Khanzada and N. Hilal, in *Water Treatment*, CRC Press, 2025, pp. 82–108.
14 L.-l. Yu, L.-n. Jiang, S.-y. Wang, M.-m. Sun, D.-q. Li and G.-m. Du, *Int. J. Biol. Macromol.*, 2018, **112**, 383–389.
15 N. R. Singha, M. Mahapatra, M. Karmakar, H. Mondal, A. Dutta, M. Deb, M. Mitra, C. Roy, P. K. Chattopadhyay and D. K. Maiti, *ACS Omega*, 2018, **3**, 4163–4180.
16 O. A. Attallah, M. A. Al-Ghobashy, M. Nebsen and M. Y. Salem, *RSC Adv.*, 2016, **6**, 11461–11480.
17 C. Cui, D. Li and L.-j. Wang, *Sep. Purif. Technol.*, 2025, **363**, 132034.
18 S. Sekar, S. E. Panchu, H. C. Swart, M. B. Sridharan and N. K. Subbaraya, *Langmuir*, 2025, **41**, 14689–14706.
19 P. Kalegowda, A. S. Chauhan and S. M. N. Urs, *Carbohydr. Polym.*, 2017, **157**, 1057–1064.
20 A. A. Kadam, B. Sharma, G. D. Saratale, R. G. Saratale, G. S. Ghodake, B. M. Mistry, S. K. Shinde, S. C. Jee and J.-S. Sung, *Cellulose*, 2020, **27**, 3301–3318.
21 V. Vigneswararajah, N. Thavarajah and X. Fernando, *Technologies*, 2025, **13**, 403.
22 Z. Shui, L. Yao, X. Pu, L. Yang, W. Jiang and X. Jiang, *Ind. Eng. Chem. Res.*, 2020, **59**, 14616–14624.
23 D. Chakraborty, A. Yurdusen, G. Mouchaham, F. Nouar and C. Serre, *Adv. Funct. Mater.*, 2024, **34**, 2309089.
24 K. Khabibi, N. A. I. Aanisa, N. B. A. Prasetya and R. A. Lusiana, *J. Membr. Sci. Res.*, 2026, **12**, e728571.
25 N. Ortega, M. Perez-Mateos, M. C. Pilar and M. D. Busto, *J. Agric. Food Chem.*, 2009, **57**, 109–115.
26 C. Chang, Z.-C. Wang, C.-Y. Quan, H. Cheng, S.-X. Cheng, X.-Z. Zhang and R.-X. Zhuo, *J. Biomater. Sci. Polym. Ed.*, 2007, **18**, 1591–1599.
27 M.-A. Shahbazi, M. Ghalkhani and H. Maleki, *Adv. Eng. Mater.*, 2020, **22**, 2000033.
28 E. Guibal, *Sep. Purif. Technol.*, 2004, **38**, 43–74.
29 K. Foo and B. H. Hameed, *Desalination Water Treat.*, 2010, **19**, 255–274.
30 G. Pasparakis and N. Bouropoulos, *Int. J. Pharm.*, 2006, **323**, 34–42.
31 H. Asranudin, A. Setyo Purnomo, H. Bahruji, D. Allouss, R. S. Ilias El Alaoui-Elbalrhiti, A. A. Rohmaha and D. Prasetyoko, *RSC Adv.*, 2023, **13**, 790–801.
32 N. I. I. Zamri, S. L. N. Zulmajdi, N. Z. A. Daud, A. H. Mahadi, E. Kusrini and A. Usman, *SN Appl. Sci.*, 2021, **3**, 1–16.
33 J. Liu, L. Wu and X. Chen, *Desalin. Water Treat.*, 2015, **54**, 2307–2313.
34 M. Vakili, M. Rafatullah, B. Salamatinia, A. Z. Abdullah, M. H. Ibrahim, K. B. Tan, Z. Gholami and P. Amouzgar, *Carbohydr. Polym.*, 2014, **113**, 115–130.
35 M. Dash, F. Chiellini, R. M. Ottenbrite and E. Chiellini, *Prog. Polym. Sci.*, 2011, **36**, 981–1014.
36 M. G. A. Vieira, M. A. Da Silva, L. O. Dos Santos and M. M. Beppu, *Eur. Polym. J.*, 2011, **47**, 254–263.
37 Q. Lin, Y. Zhou, S. Ma, S. Lin, Y. Cai, Z. Huang, S. Miao and X. Lu, *J. Future Foods*, 2025, DOI: 10.1016/j.jfutfo.2025.10.038.
38 B. R. Thakur, R. K. Singh, A. K. Handa and M. Rao, *Crit. Rev. Food Sci. Nutr.*, 1997, **37**, 47–73.
39 K. Y. Lee and D. J. Mooney, *Prog. Polym. Sci.*, 2012, **37**, 106–126.
40 G.-W. Oh, S. Y. Nam, S.-J. Heo, D.-H. Kang and W.-K. Jung, *Int. J. Biol. Macromol.*, 2020, **156**, 1565–1573.
41 S. Seslija, D. Veljovic, M. K. Krusic, J. Stevanovic, S. Velickovic and I. Popovic, *New J. Chem.*, 2016, **40**, 1618–1625.
42 Z. Ahmadian, M. Z. Jelodar, M. Rashidipour, M. Dadkhah, V. Adhami, S. Sefareshi, H. A. Ebrahimi, M. Ghasemian and M. Adeli, *Daru J. Pharm. Sci.*, 2023, **31**, 205–219.
43 J. A. Figueirôa, G. U. M. Novaes, H. de Souza Gomes, V. L. M. de Morais Silva, D. de Moraes Lucena, L. M. R. Lima, S. A. de Souza, L. G. F. C. Viana, L. A. Rolim and J. R. G. da Silva Almeida, *Heliyon*, 2021, 7.

44 Y. Boumezough, G. Viscusi, S. Arris, G. Gorrasi and S. A. Carabineiro, *Int. J. Mol. Sci.*, 2025, **26**, 6717.

45 R. G. Huamani-Palomino, M. Pedro Ramos, G. Oliveira, F. V. C. Kock, T. Venâncio and B. M. Córdova, *Biomass Convers. Biorefin.*, 2025, **15**, 2047–2061.

46 A. Saarai, T. Sedlacek, V. Kasparkova, T. Kitano and P. Saha, *J. Appl. Polym. Sci.*, 2012, **126**, E79–E88.

47 M. Filippov, *J. Appl. Spectrosc.*, 1972, **17**, 1052–1054.

48 Z. Zhao, C. Geng, X. Zhao, Z. Xue, F. Quan and Y. Xia, *Nanomaterials*, 2019, **9**, 570.

49 S. X. Tiew and M. Misran, *J. Appl. Polym. Sci.*, 2017, **134**, 44849.

50 S. Wang, J. Dou, T. Zhang, S. Li and X. Chen, *ACS Omega*, 2023, **8**, 35024–35033.

51 J. Liu, Q.-h. Zhang, F. Ma, S.-f. Zhang, Q. Zhou and A.-m. Huang, *J. Mol. Struct.*, 2020, **1218**, 128484.

52 Y. Zhan, L. Yang, J. Lan, J. Shang, S. Chen, X. Guan, W. Li and S. Lin, *Cellulose*, 2021, **28**, 453–470.

53 N. E. Williams, O. A. Oba and N. P. Aydinlik, *ChemBioEng Rev.*, 2022, **9**, 164–189.

54 H. N. Tran, S.-J. You and H.-P. Chao, *Korean J. Chem. Eng.*, 2017, **34**, 1708–1720.

55 S. Suganthi, S. Vignesh, M. M. Al-Ansari, L. A. Al-Humaid, T. H. Oh and V. Raj, *Polym. Adv. Technol.*, 2024, **35**, e6413.

56 I. Pitterou, F. Kalogeropoulou, A. Tzani, K. Tsiantas, M. A. Gatou, E. Pavlatou, A. Batrinou, C. Fountzoula, A. Kriebardis and P. Zoumpoulakis, *Molecules*, 2024, **29**, 5318.

57 H. H. Phan and A. N. Phan, in *Biomass-Based Functional Carbon Nanostructures for Supercapacitors*, Springer, 2023, pp. 179–221.

58 A. Pawlak and M. Mucha, *Thermochim. Acta*, 2003, **396**, 153–166.

59 R. Bao, X. He, Y. Liu, Y. Meng and J. Chen, *Coatings*, 2023, **13**, 516.

60 D. de Britto and S. P. Campana-Filho, *Thermochim. Acta*, 2007, **465**, 73–82.

61 S. H. Ching, N. Bansal and B. Bhandari, *Crit. Rev. Food Sci. Nutr.*, 2017, **57**, 1133–1152.

62 S. Hydari, H. Sharififard, M. Nabavinia and M. reza Parvizi, *Chem. Eng. J.*, 2012, **193**, 276–282.

63 P. Chamnannetivit, S. Phrommachan and C. Umpuch, *J. Dispersion Sci. Technol.*, 2024, 1–17.

64 A. Zhou, Q. Wu, H. Zhang, J. Liu, C. Wang, D. Chi and H. Zhou, *J. Environ. Manag.*, 2026, **401**, 128837.

65 K. Foo and B. H. Hameed, *Desalin. Water Treat.*, 2010, **19**, 255–274.

66 M. A. Khapre, S. Pandey and R. M. Jugade, *Int. J. Biol. Macromol.*, 2021, **190**, 862–875.

67 G. Chen, Y. Yin, X. Zhang, A. Qian, X. Pan, F. Liu and R. Li, *Molecules*, 2024, **29**, 1836.

68 N. Loc, P. Tuyen, L. Mai and D. Phuong, *Toxics*, 2022, **10**, 500.

69 U. Ghani, W. Jiang, K. Hina, A. Idrees, M. Iqbal, M. Ibrahim, R. Saeed, M. K. Irshad and I. Aslam, *Front. Environ. Sci.*, 2022, **10**, 887425.

70 X. Cheng, D. Jiang, H. Chen, B. Barati, C. Yuan, H. Li and S. Wang, *Chemosphere*, 2023, **338**, 139218.

71 S.-P. Zhao, F. Zhou and L.-Y. Li, *J. Polym. Res.*, 2012, **19**, 9944.

72 A. H. Jawad, N. H. Mamat, B. Hameed and K. Ismail, *J. Environ. Chem. Eng.*, 2019, **7**, 102965.